

# Characterizing turbulence in galaxy clusters: defining turbulent energies and assessing multi-scale versus fixed-scale filters

Lorenzo Maria Perrone<sup>1</sup>, Thomas Berlok<sup>2,1</sup>, Ewald Puchwein<sup>1</sup>, and Christoph Pfrommer<sup>1</sup>

<sup>1</sup> Leibniz-Institut für Astrophysik Potsdam (AIP), An der Sternwarte 16, D-14482 Potsdam, Germany  
e-mail: 1perrone@aip.de

<sup>2</sup> Niels Bohr Institute, University of Copenhagen, Blegdamsvej 17, 2100 Copenhagen, Denmark

January 13, 2026

## ABSTRACT

Disentangling turbulence and bulk motions in the intracluster medium (ICM) of galaxy clusters is inherently ambiguous, as the plasma is continuously stirred by different processes on disparate scales. This poses a serious problem in the interpretation of both observations and numerical simulations. In this paper, we use filtering operators in real space to separate bulk motion from turbulence at different scales. We show how filters can be used to define consistent kinetic and magnetic energies for the bulk and turbulent component. We apply our GPU-accelerated filtering pipeline to a simulation of a major galaxy cluster merger, which is part of the PICO-CLUSTERS suite of zoom-in cosmological simulations of massive clusters using the moving mesh code AREPO and the ILLUSTRISTNG galaxy formation model. We find that during the merger the turbulent pressure fraction on physical scales  $\lesssim 160$  kpc reaches a maximum of 5%, before decreasing to 2% after  $\sim 1.3$  Gyr from the core passage. These low values are consistent with recent observations of clusters with XRISM, and suggest that unless a cluster was recently perturbed by a major merger, turbulence levels are low. We then re-examine the popular multiscale iterative filter method. In our tests, we find that its use can introduce artifacts, and that it does not reliably disentangle fluctuations living on widely separated length scales. Rather, we believe it is more fruitful to use fixed-scale filters and turbulent energies to compare between simulations and observations. This work significantly improves our understanding of turbulence generation by major mergers in galaxy clusters, which can be probed by XRISM and next-generation X-ray telescopes, allowing us to connect high-resolution cosmological simulations to observations.

**Key words.** Galaxies: clusters: intracluster medium – Turbulence – Magnetohydrodynamics (MHD) – Plasmas – Methods: numerical

## 1. Introduction

The intracluster medium (ICM) that fills galaxy clusters is a hot and diffuse plasma, where motions are excited by different physical mechanisms on a wide range of temporal and spatial scales (Simionescu et al. 2019). While constraining the Reynolds number of such a medium remains an area of open investigation (Werner et al. 2016; Su et al. 2017; Wang & Markevitch 2018; Zhuravleva et al. 2019; XRISM Collaboration et al. 2025a), the ICM is understood to be turbulent, with density and velocity fluctuations probed down to scales of  $\lesssim 10$  kpc (Walker et al. 2015). The presence of turbulence has major implications for a number of physical processes, including, but not limited to, the amplification of magnetic fields through a small-scale dynamo, and its keeping at approximate equipartition levels with the turbulence (Schekochihin et al. 2004; Beresnyak & Miniati 2016; Domínguez-Fernández et al. 2019; St-Onge et al. 2020; Tevlin et al. 2025); the re-acceleration of relativistic electrons that are thought to produce the diffuse radio emission detected even at megaparsec-scale distances from the cluster center, as seen in radio observations (Cuciti et al. 2022; Botteon et al. 2022; Beduzzi et al. 2023, 2024; Rajpurohit et al. 2025) and modeled theoretically and in simulations (Brunetti & Lazarian 2007; Pinzke et al. 2017); the turbulent heating of the ICM through dissipation of small-scale turbulence, which might contribute to offset radiative cooling in certain parts of the cluster (Kunz et al. 2011; Zhuravleva et al. 2014a; Yang & Reynolds 2016); the non-thermal contribution to pressure support in the cluster, leading to hydrostatic

mass bias (Lau et al. 2009; Battaglia et al. 2012; Eckert et al. 2019; Angelinelli et al. 2020); and, more generally, for our understanding of the effects of kinetic-scale plasma instabilities on macroscopic transport processes (Zhuravleva et al. 2019; Berlok et al. 2021; Drake et al. 2021; Perrone et al. 2024; Perrone et al. 2024; Yerger et al. 2025; Choudhury & Bott 2025) and on the turbulent cascade (Schekochihin & Cowley 2006; Squire et al. 2019, 2023; Arzamasskiy et al. 2023; Majeski et al. 2024).

Despite its importance for the formation and evolution of galaxy clusters, the properties of turbulence in the ICM are still not well understood. With the recent deployment of the XRISM X-ray microcalorimeter (and previously with Hitomi), it has finally become possible to directly probe small-scale gas velocities through measurements of turbulent line broadening (Hitomi Collaboration et al. 2016). The first results indicate turbulent velocity amplitudes of the order of  $100 - 200$  km s $^{-1}$  in the central part of the cluster, with no obvious trend with respect to its dynamical state, i.e. whether it is a relaxed cluster or undergoing a major merger (XRISM Collaboration et al. 2025a). These values, corresponding to a turbulent pressure support of 2–4% (XRISM Collaboration et al. 2025d,b), are generally on the lower end of previous estimates obtained with X-ray spectrometers, although these measurements likely include contributions from different spatial scales, and in general the role of instrumental effects or data-reduction techniques is yet to be fully clarified (Lau et al. 2017; ZuHone et al. 2018; Groth et al. 2025; Vazza & Brunetti 2025).

The increased availability of state-of-the-art observations of several nearby clusters calls for a corresponding effort from the simulation side to develop a more comprehensive understanding of the drivers of turbulence and its evolution throughout cosmic time, in order to compare to observational data and constrain the physical models used to both simulate and interpret the observations. A major stumbling block is the inherent ambiguity of defining what is turbulence in such a highly inhomogeneous environment, like the ICM, which is radially stratified and where motions are stirred from megaparsec scales by cluster mergers (Miniati 2015), down to scales of  $\sim 10$  kpc by the central AGN (Bourne & Sijacki 2017; Ehlert et al. 2021) in combination with radiatively cooling gas (Ehlert et al. 2023) or MHD instabilities driven by anisotropic heat conduction (Perrone & Latter 2022), and further below by kinetic plasma instabilities at observationally inaccessible scales comparable to the ion Larmor radius ( $\sim 10^{-9}$  pc) (Schekochihin et al. 2005; Kunz et al. 2014; Roberg-Clark et al. 2018; Komarov et al. 2018; Ley et al. 2024).

Different approaches have been employed to estimate the levels of ICM turbulence in numerical simulations and observations of galaxy clusters. Examples are spherical-shell averaging or fitting (Zhuravleva et al. 2013, 2014a; Romero et al. 2024), three-dimensional interpolation using shape functions (Dolag et al. 2005; Valdarnini 2011; Vazza et al. 2011), sub-grid modeling (Scannapieco & Brüggen 2008; Iapichino et al. 2011), power spectra estimators (Gaspari et al. 2014; Zhuravleva et al. 2014b; Shi et al. 2018; Wang & He 2024b) and structure functions (Matiati 2014; Beresnyak & Miniti 2016; Li et al. 2020; Wang et al. 2021). In this work, we argue for an approach based on fixed-scale filtering and the computation of turbulent energies via statistical moments. We implement this method in a Python package which we parallelize for GPUs to handle large datasets efficiently. As a practical example, we apply it to a massive merging cluster from the PICO-CLUSTERS simulation suite (Berlok et al. in prep., Tevlin et al. 2025) run with the AREPO code (Springel 2010; Pakmor et al. 2016), that includes magnetic fields (Pakmor et al. 2011; Pakmor & Springel 2013), radiative cooling and heating, as well as the ILLUSTRIS-TNG galaxy formation model (Weinberger et al. 2017; Pillepich et al. 2018). With this method we can extract detailed information on how much turbulence is generated during the merger and how it is partitioned on different scales. We also revisit the iterative multiscale filtering technique (Vazza et al. 2012), which is a method that has gained traction in the community to separate bulk from turbulence and automatically identify the (spatially-varying) integral/correlation scale of the turbulence in different parts of the cluster. We find that the detection of turbulence by iterative filters can often be unreliable even in simple test cases. For this reason, we believe they hinder the physical interpretation of the data, rather than clarify it, thereby making the fixed-scale filtering and the computation of the filtered energies our favored approach.

This paper is structured as follows: in Section 2 we discuss different filtering operators; in Section 3 we introduce the notations for turbulent magnetic and kinetic energies through statistical moments, and examine their relation to the energy of small-scale fluctuations. We then show in Section 4 the results of this decomposition to a massive merging cluster. Finally, in Section 5 we analyze the iterative multiscale filters and highlight their potential pitfalls. We draw our conclusions in Section 6, and we outline the prospects for future work.

The main text is complemented by the following Appendices: in Appendix A we compare two widely used filters in Fourier space and examine their convergence with iterative multiscale filters; in Appendix B we prove several useful mathematical results concerning the operations of volume averaging and filtering; in Appendix C we show how the filtered energies change under Galilean transformations, and study the limit of subsonic turbulence; in Appendix D we describe our numerical pipeline for filtering cosmological simulations; finally, in Appendix E, we derive an expression for the turbulent energy in non-periodic domains.

mathematical results concerning the operations of volume averaging and filtering; in Appendix C we show how the filtered energies change under Galilean transformations, and study the limit of subsonic turbulence; in Appendix D we describe our numerical pipeline for filtering cosmological simulations; finally, in Appendix E, we derive an expression for the turbulent energy in non-periodic domains.

## 2. Filtering operators

### 2.1. Mathematical preliminaries

In the study of turbulence, it is often useful to extract the statistical properties of chaotic fields by applying different types of mathematical operators, such as time or spatial averaging. Under the assumption of ergodicity averaging operators can be used in lieu of ensemble averaging, making them a practical tool to study chaotic flows (see, e.g., discussion in Frisch 1995).

A more general class of averaging operators are the filtering operators, which can be thought of as a convolution integral of the physical field with a kernel in time or space (Germano 1992). In this work we will focus on filtering operators in real space, defined by a kernel  $W_\ell(\mathbf{x}', \mathbf{x})$  parametrized by the smoothing length  $\ell$ . Furthermore we assume that the filtering kernel is positive definite, normalized to unity, and centered around  $\mathbf{x}$ :

$$W_\ell(\mathbf{x}', \mathbf{x}) \geq 0, \quad (1a) \quad \int W_\ell(\mathbf{x}', \mathbf{x}) d^3 x' = 1, \quad (1b)$$

$$\int \mathbf{x}' W_\ell(\mathbf{x}', \mathbf{x}) d^3 x' = \mathbf{x}. \quad (1c)$$

where, unless otherwise specified, the integration is carried out over the entire space. The application of such a filter in position space, denoted by  $\langle \dots \rangle_\ell$ , can be written as

$$\langle f \rangle_\ell(\mathbf{x}) \equiv \int f(\mathbf{x}') W_\ell(\mathbf{x}', \mathbf{x}) d^3 x'. \quad (2)$$

Seen in spectral space, the effect of filtering is to suppress the power on certain scales but not others, depending on the shape of the kernel. In this paper we only deal with filters that leave the power on spatial scales larger than  $\ell$  unchanged (low-pass filters), hence the name “smoothing filters”. Thus, the filtering approach allows us to decompose a physical field into the sum of its smooth  $\langle f \rangle_\ell(\mathbf{x})$  and fluctuating  $\delta f_\ell(\mathbf{x}) = f(\mathbf{x}) - \langle f \rangle_\ell(\mathbf{x})$  components at each point in space. The usual spatial average over a finite volume  $V$ ,

$$\langle f \rangle_V \equiv \frac{1}{V} \int_V f(\mathbf{x}') d^3 x'. \quad (3)$$

can be understood as a special case of a filtering kernel, with a constant value when  $\mathbf{x}' \in V$  and zero outside. The advantage of smoothing kernels over simple spatial averages is that they are local, i.e., the value of the filtered variable now depends on the position  $\mathbf{x}$  and reflects the conditions in a specific part of the domain (we will drop the explicit dependence of the filtered fields on  $\mathbf{x}$  when there is no risk of ambiguity).

One disadvantage compared to spatial averages is that filtering operators do not satisfy the Reynolds rules of averaging,

$$\langle f \langle g \rangle_V \rangle_V = \langle f \rangle_V \langle g \rangle_V, \quad (4)$$

where  $f(\mathbf{x})$  and  $g(\mathbf{x})$  are generic fields (see, e.g., Monin & Yaglom 1971). In particular, repeatedly applying the smoothing filter to the smooth component affects its value, and filtering the

fluctuating component does not yield zero. For our purposes, a consequence of Eq. (4) is that it allows us to decompose the energy of a field (e.g., the magnetic field) into the sum of the energies of the constant-in-space volume average  $\langle \mathbf{B} \rangle_V$  and its spatially-varying fluctuating component  $\delta \mathbf{B} = \mathbf{B} - \langle \mathbf{B} \rangle_V$ , respectively:

$$E_B \equiv \int_V \frac{\mathbf{B}^2}{8\pi} d^3x = \int_V \frac{\langle \mathbf{B} \rangle_V^2}{8\pi} d^3x + \int_V \frac{\delta \mathbf{B}^2}{8\pi} d^3x. \quad (5)$$

As we show in Section 3, this decomposition does not hold true for a general filtering operator that satisfies Eq. (1), as in this case several terms in the form of  $\langle f \langle g \rangle_\ell \rangle_\ell$  appear, which cannot be simplified as  $\langle f \rangle_\ell \langle g \rangle_\ell$ . This is the reason why a different formalism must be employed when computing the energies of the bulk component and of the fluctuations (Germano 1992).

In this work we consider the following smoothing kernels (written here for  $n = 1, 2, 3$  dimensions): the spherical top-hat filter,

$$\mathcal{W}_\ell(\mathbf{x}', \mathbf{x}) = \begin{cases} \Omega_n^{-1} & \text{if } |\mathbf{x} - \mathbf{x}'| \leq \ell, \\ 0 & \text{if } |\mathbf{x} - \mathbf{x}'| > \ell, \end{cases} \quad (6)$$

where  $\Omega_n = (\ell \sqrt{\pi})^n / \Gamma(n/2+1)$  is the volume of an  $n$ -dimensional sphere ( $\Gamma(z)$  is the gamma function), such that  $\Omega_1 = 2\ell$ ,  $\Omega_2 = \pi\ell^2$ , and  $\Omega_3 = (4/3)\pi\ell^3$  in one, two and three dimensions, respectively; and the Gaussian filter,

$$\mathcal{W}_\ell(\mathbf{x}', \mathbf{x}) = \frac{1}{(2\pi\ell^2)^{n/2}} e^{-\frac{1}{2}|\mathbf{x} - \mathbf{x}'|^2/\ell^2}, \quad (7)$$

where in practice we truncate the support of the Gaussian to  $|\mathbf{x} - \mathbf{x}'| \leq 4\ell$ . For their representation in Fourier space we refer to Appendix A. These kernels are functions of the distance  $|\mathbf{x} - \mathbf{x}'|$  only, which makes them isotropic around  $\mathbf{x}$ . In most scenarios, the physical fields that we wish to filter are defined in a finite domain corresponding, e.g., to the entire box of a numerical simulation (that may or may not be periodic) or to a smaller subvolume  $V$  thereof, which corresponds to our case. As a result, to satisfy Eq. (1), when we apply the smoothing filter we require information on the physical fields not only in  $V$ , but also in a buffer region  $\delta V$  around  $V$  that contains the support of  $\mathcal{W}_\ell$  for points near its boundaries. An alternative approach is to restrict the integration to  $V$  only; however, to satisfy the normalization condition, the smoothing kernel cannot in general be symmetric (or centered) around  $\mathbf{x}$  near the boundaries (Eq. 1c). For further discussion, refer to Appendix B.

Throughout the paper, we will often refer to the ‘‘cutoff’’ filter length ( $\lambda_c$ ) for each filter, which we take to be the half-width at half-maximum in wavenumber space (i.e., the wavelength at which the Fourier amplitude is attenuated by a factor of 1/2).<sup>1</sup> For different kernels,  $\lambda_c$  is related to the filter length  $\ell$  by a unique numerical coefficient, which takes into account the fact that for the same nominal  $\ell$  different kernels can have very dissimilar shapes in wavenumber space (see Appendix A). We implement our filtering pipeline in Python using the Numba-CUDA library to allow fast computations on NVIDIA graphical processing units (GPUs). For further numerical details on the implementation, see Appendix D.

<sup>1</sup> For a Gaussian filter, the cutoff filter length ( $\lambda_c$ ) and smoothing length ( $\ell$ ) are related via  $\lambda_c/\ell = 2\pi/\sqrt{2\ln 2} \approx 5.33645$  (see App. A.1).

## 2.2. Filtering of a cosmological simulation

To illustrate a practical application, we show the result of filtering in a cosmological simulation of a massive galaxy cluster, dubbed ‘‘Halo3’’. The simulation is part of the PICO-CLUSTERS suite of zoom-in galaxy cluster simulations (Berlok et al. in prep., Tevlin et al. 2025) performed with the moving-mesh code AREPO (see Section 4.1 for more details on the setup). To simplify the numerics, the AREPO code evolves the ideal MHD equations using comoving quantities in a uniformly expanding space-time defined by the Hubble function  $H(a) = \dot{a}/a$ , where  $a$  is the scale factor of the universe, and the dot represents the time derivative (Pakmor & Springel 2013; Weinberger et al. 2020); see, e.g., Appendix B in Berlok (2022) for a derivation of the comoving MHD equations. For instance, the Hubble flow due to the expansion of the Universe  $H(a)\mathbf{r}$ , where  $\mathbf{r}$  is the physical position vector, is subtracted from the total (physical) velocity  $\mathbf{u}$ , and only the comoving ‘‘peculiar’’ velocity  $\mathbf{v}$  is evolved:

$$\mathbf{v} \equiv a\dot{\mathbf{x}} = \mathbf{u} - H(a)\mathbf{r}, \quad (8)$$

where  $\mathbf{x} = \mathbf{r}/a$  is the comoving position. However, here and in the rest of the paper it is understood that all quantities are shown in physical (non-comoving) units. In particular, unless otherwise stated, we always compute the physical velocity  $\mathbf{u}$  with respect to the center of mass of Halo3 and not the peculiar velocity.

In Fig. 1, we plot the total, bulk and turbulent components of the density, velocity and magnetic field, respectively, of Halo3 at redshift  $z = 0.51$  before a major merger with a second massive cluster ( $M_{200,c} \simeq 5.38 \times 10^{14} \text{ M}_\odot$  vs.  $1.30 \times 10^{15} \text{ M}_\odot$  for Halo3), where  $M_{200,c}$  refers to the mass contained within the virial radius  $R_{200,c}$ , such that the mean density inside this sphere is 200 times the critical density. The smoothing kernel is Gaussian, with a physical smoothing length of  $\ell = 30 \text{ kpc}$  ( $\lambda_c \simeq 160 \text{ kpc}$ ). We define the smooth (bulk) and turbulent components of gas mass density, gas velocity and magnetic field as:

$$\rho = \langle \rho \rangle_\ell + \delta \rho_\ell, \quad \mathbf{u} = \langle \mathbf{u} \rangle_\ell + \delta \mathbf{u}_\ell, \quad \mathbf{B} = \langle \mathbf{B} \rangle_\ell + \delta \mathbf{B}_\ell. \quad (9)$$

At the time of the snapshot in Fig. 1, the cluster is still relatively relaxed, with a roughly spherical density distribution and low ( $\lesssim 600 \text{ km s}^{-1}$ ) total velocities in the core region. There is a stark difference between the amplitudes of the total fields and the turbulent fluctuations. Filtering of the density field reveals inhomogeneous density fluctuations in the clusters: their absolute amplitude progressively decreases moving radially away from the center, and their morphology also changes from being spherically symmetric in the core region, to being more isotropic further out. Looking at the velocity fluctuations, we find that they amount to less than  $200 \text{ km s}^{-1}$  within the inner megaparsec region, which is about a third of the total/bulk fields. The opposite is true for the magnetic fields, as the amplitudes of the turbulent fluctuations is instead larger than that of the bulk field. Finally, we see an increase of the amplitude of the velocity fluctuations with radius in agreement with previous studies (Shi et al. 2018).

## 3. Definition of turbulent energies

Having introduced the smoothing filters, we now introduce a way to define turbulent and bulk energies within the filtering approach that is both mathematically sound and physically meaningful. The solution comes from the generalized statistical moments of turbulent fields, which constitutes the cornerstone of large-eddy simulations (LES) of hydrodynamic turbulence (Leonard 1974; Rogallo & Moin 1984). In particular, by

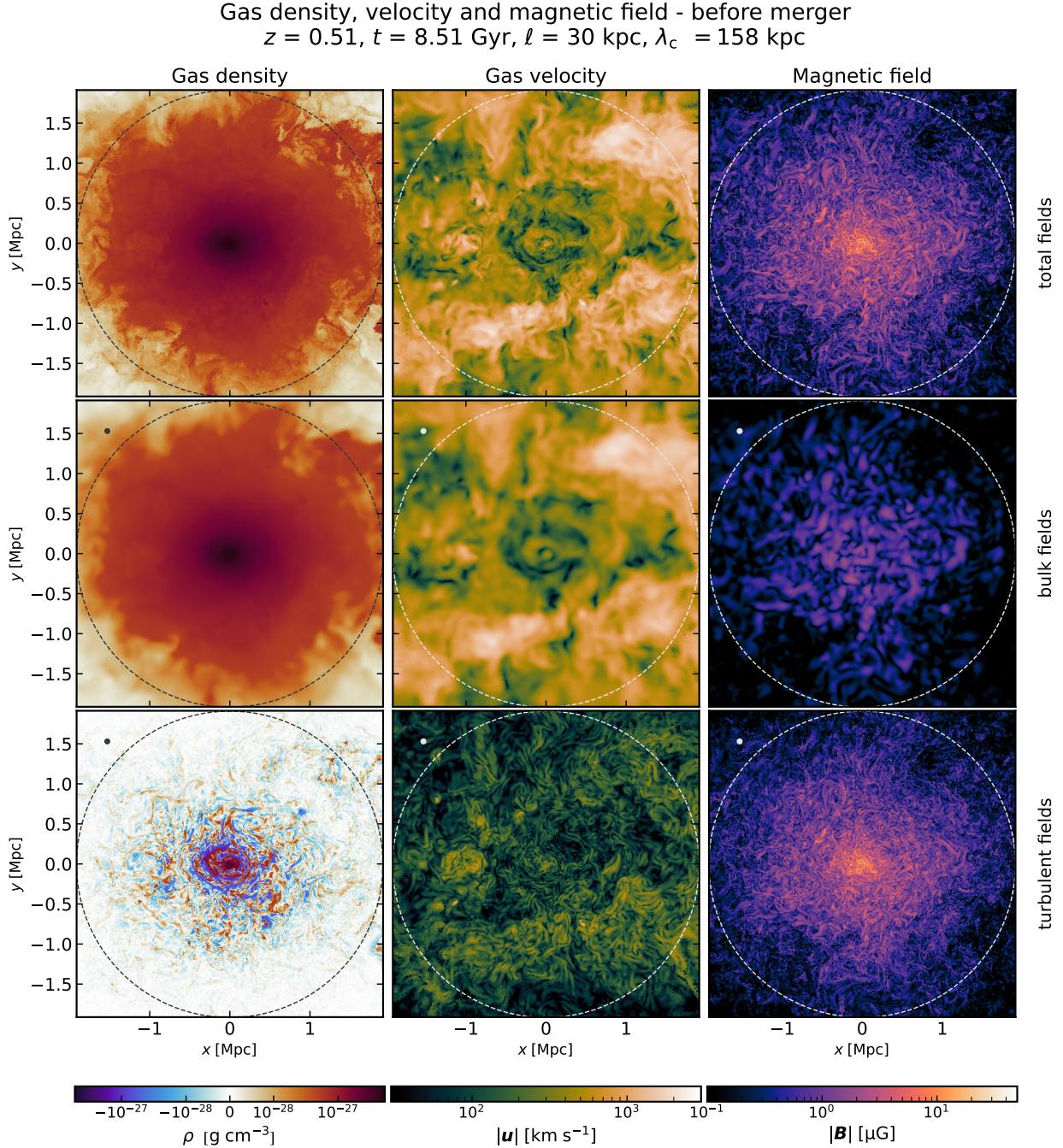


Fig. 1: Decomposition of the gas density, gas velocity and magnetic field of *Halo3* before the merger ( $z = 0.51$ ) for a filter scale of  $\ell = 30$  kpc (represented by a beam of radius  $\ell$  in the top left corner). From top to bottom: slices of the total field, bulk and turbulent components across the center of the cluster. The coordinates are in physical units with respect to the center of mass of the cluster, while dashed lines denote the virial radius  $R_{200,c}$ . The colorbars are in common for each column. The cluster appears to be relatively relaxed, with a roughly spherical shape.

introducing second- and third-order statistical moments  $\mu_2(f, g)$  and  $\mu_3(f, g, h)$ , defined as

$$\mu_2(f, g) = \langle fg \rangle_\ell - \langle f \rangle_\ell \langle g \rangle_\ell, \quad (10)$$

$$\mu_3(f, g, h) = \langle fgh \rangle_\ell - \langle f \rangle_\ell \mu_2(g, h) - \langle g \rangle_\ell \mu_2(h, f) - \langle h \rangle_\ell \mu_2(f, g) - \langle f \rangle_\ell \langle g \rangle_\ell \langle h \rangle_\ell, \quad (11)$$

where  $f(\mathbf{x}), g(\mathbf{x}), h(\mathbf{x})$  are generic turbulent fields, it is possible to define generalized turbulent energies, as well as their evolution equations (Germano 1992; Eyink 2007). Note that  $f, g$ , and

$h$ , can be vectors, in which case  $\mu_2, \mu_3$  are higher-rank tensors. These statistical moments can be thought of as the correlation between the turbulent components of different fields, and vanish identically if any one of the arguments is a constant (in fact, this is the case for statistical moments of any order as can be shown, e.g., by induction). For a scalar field  $\rho$ , its second-order statistical moment with itself  $\mu_2(\rho, \rho)$  can be loosely interpreted as the variance of the field. A similar argument applies to a vector field  $\mathbf{u}$  with the trace of the tensor  $\mu_2(u_i, u_j) = \langle u_i u_j \rangle_\ell - \langle u_j \rangle_\ell \langle u_j \rangle_\ell$ . It is

worth noting that in the context of LES the full tensor  $\mu_2(u_i, u_j)$  is known as the subgrid-scale stress tensor (see Section 3.5 for further discussion on the connections with LES).

In this work, we follow closely the approach of Hollins et al. (2022) for the definitions of the kinetic and magnetic bulk and turbulent energies. The form of these relations depends on whether we are considering the magnetic or kinetic energy, since they involve second- or third-order correlations, respectively. We report them here below for convenience. To avoid confusion, throughout the paper we employ the  $\mathcal{E}$  and  $\varepsilon$  to refer to the filtered energies and filtered energy densities, respectively, based on the statistical moments, while we use upper-case  $E$  and lower-case  $e$  whenever we refer to the commonplace definitions of energies and energy densities, respectively, e.g.,  $e_B = \mathbf{B}^2/8\pi$  and  $e_k = \rho\mathbf{u}^2/2$  for the magnetic and kinetic energy density, respectively.

### 3.1. Magnetic energy

We consider a decomposition of the magnetic field into a smooth and fluctuating component (Eq. 9) with a smoothing filter of scale  $\ell$ . Filtering the magnetic energy density  $e_B = \mathbf{B}^2/8\pi$  leads to the following identity

$$\mathcal{E}_B = \mathcal{E}_{B,\text{bulk}} + \mathcal{E}_{B,\text{turb}}, \quad (12)$$

where  $\mathcal{E}_B = \langle e_B \rangle_\ell$  is the filtered energy density of the total field,  $\mathcal{E}_{B,\text{bulk}}$  is the energy density of the smooth magnetic field and  $\mathcal{E}_{B,\text{turb}}$  is the filtered energy density of the fluctuations:

$$\mathcal{E}_B = \frac{\langle \mathbf{B}^2 \rangle_\ell}{8\pi}, \quad \mathcal{E}_{B,\text{bulk}} = \frac{\langle \mathbf{B}_\ell^2 \rangle}{8\pi}, \quad \mathcal{E}_{B,\text{turb}} = \frac{\sum_i \mu_2(B_i, B_i)}{8\pi}, \quad (13)$$

where  $\mu_2$  is the second-order statistical moment of the magnetic field defined in Eq. (10), and the sum runs over the spatial indices  $i = x, y, z$ . For ease of reading, we dropped the subscript  $\ell$  in the notation of the filtered energy densities (Eqs. 12-13), but it is understood that they depend on the value of the filtering length. Integrating the filtered energy densities over the entire volume, one arrives at the following definitions of the filtered energies:

$$\begin{aligned} \mathcal{E}_B &= \int_V \mathcal{E}_B d^3x, & \mathcal{E}_{B,\text{bulk}} &= \int_V \mathcal{E}_{B,\text{bulk}} d^3x, \\ \mathcal{E}_{B,\text{turb}} &= \int_V \mathcal{E}_{B,\text{turb}} d^3x, \end{aligned} \quad (14)$$

which satisfy

$$\mathcal{E}_B = \mathcal{E}_{B,\text{bulk}} + \mathcal{E}_{B,\text{turb}}. \quad (15)$$

Before proceeding further, it is worth stressing several fundamental aspects; first, the filtered energy densities, as defined in Eq. (13) are conceptually different from what one would naively define as the energy densities of the total ( $\mathbf{B}^2/8\pi$ ), bulk ( $\langle \mathbf{B} \rangle_\ell^2/8\pi$ ) and fluctuating magnetic field ( $\delta\mathbf{B}_\ell^2/8\pi$ ). Only the energy density of the smooth field is the same:  $\mathcal{E}_{B,\text{bulk}} = \langle \mathbf{B}_\ell^2 \rangle/8\pi$ . The distinction is important, since the naively bulk and turbulent energy densities do not sum up meaningfully, while the filtered energy densities in Eq. (12) do by construction (Hollins et al. 2022). In the same spirit, it is instructive to compare the filtered turbulent energy  $\mathcal{E}_{B,\text{turb}}$  with the analogous expression from Eq. (5) obtained via volume-averaging. We start by rewriting the second-order statistical moment  $\mu_2$  using the definition in Eq. (10) as

$$\begin{aligned} \sum_i \mu_2(B_i, B_i) &= \langle \mathbf{B}^2 \rangle_\ell - \langle \mathbf{B}_\ell^2 \rangle = \langle (\langle \mathbf{B} \rangle_\ell + \delta\mathbf{B}_\ell)^2 \rangle_\ell - \langle \mathbf{B}_\ell^2 \rangle \\ &= [\langle \delta\mathbf{B}_\ell^2 \rangle_\ell + 2\langle \delta\mathbf{B}_\ell \cdot \langle \mathbf{B} \rangle_\ell \rangle_\ell] + [\langle \langle \mathbf{B} \rangle_\ell^2 \rangle_\ell - \langle \mathbf{B}_\ell^2 \rangle_\ell]. \end{aligned} \quad (16)$$

Substituting this expression into Eq. (13) and integrating over the volume leads to a substantial simplification, whereby:

$$\mathcal{E}_{B,\text{turb}} = \int_V \frac{\delta\mathbf{B}_\ell^2}{8\pi} d^3x + \int_V \frac{2\delta\mathbf{B}_\ell \cdot \langle \mathbf{B} \rangle_\ell}{8\pi} d^3x, \quad (17)$$

where we used the fact that the last square bracket of Eq. (16) vanishes when integrated over  $V$  if the domain is periodic, or if the smoothing kernel  $\mathcal{W}_\ell(\mathbf{x}', \mathbf{x})$  is symmetric in its arguments and conserves the volume in  $V$  (see Appendix B).

Comparing Eq. (17) with the analogous expression for volume averaging from Eq. (5),

$$E_B|_{\text{turb}} = \int_V \frac{\delta\mathbf{B}^2}{8\pi} d^3x, \quad (18)$$

shows that in addition to the contribution of the naively estimate for the turbulent energy  $\delta\mathbf{B}_\ell^2/8\pi$ , in the filtering approach  $\mathcal{E}_{B,\text{turb}}$  contains a cross term proportional to the projection of the fluctuating magnetic field onto the bulk component, resulting in a higher turbulent energy if the two are preferentially aligned. Finally, we remark that the energy decomposition with smoothing filters does not encode any physical pronouncement about the nature of turbulence, i.e., the presence of chaotic random fields, but is purely a statement about the scales on which the fields vary. For instance, an ordered small-scale fluctuation (smaller than the filter size) would be classified as “turbulence” with this approach. For further discussion on the physical meaning of the filtered energies, we refer the reader to Section 3.4.

### 3.2. Kinetic energy

While in the bulk of the ICM turbulence is mostly subsonic, motions induced by mergers and sloshing can reach transonic Mach numbers  $\mathcal{M} = u/c_s \gtrsim 1$  (Simionescu et al. 2019), where  $u$  is the typical velocity amplitude and  $c_s$  is the sound speed. In this case it becomes important to include contributions from the gas density fluctuations in the computation of the filtered kinetic energy, making it a third-order statistical moment. For compressible turbulence, by decomposing the density and velocity field in terms of their smooth components and fluctuations (Eq. 9), it can be shown that the filtered kinetic energy density  $\varepsilon_k = \langle e_k \rangle_\ell$ , where

$$e_k = \frac{1}{2} \rho \mathbf{u}^2, \quad (19)$$

satisfies the following relationship:

$$\varepsilon_k = \varepsilon_{k,\text{bulk}} + \varepsilon_{k,\text{cross}} + \varepsilon_{k,\text{turb}}. \quad (20)$$

In Eq. (20),  $\varepsilon_{k,\text{bulk}}$  is the energy density of the bulk flow,

$$\varepsilon_{k,\text{bulk}} = \frac{1}{2} \langle \rho \rangle_\ell \sum_i \langle u_i \rangle_\ell \langle u_i \rangle_\ell, \quad (21)$$

$\varepsilon_{k,\text{cross}}$  is a cross term and represents the transport of the turbulent momentum by the bulk flow,

$$\varepsilon_{k,\text{cross}} = \sum_i \langle u_i \rangle_\ell \mu_2(\rho, u_i), \quad (22)$$

and  $\varepsilon_{k,\text{turb}}$  is the filtered kinetic energy density of the fluctuations,

$$\varepsilon_{k,\text{turb}} = \frac{1}{2} \langle \rho \rangle_\ell \sum_i \mu_2(u_i, u_i) + \frac{1}{2} \sum_i \mu_3(\rho, u_i, u_i), \quad (23)$$

where  $\mu_2$  and  $\mu_3$  are defined in Eqs. (10)–(11) and the sum runs over the spatial indices  $i = x, y, z$ . Together  $\varepsilon_{k,\text{cross}}$  and  $\varepsilon_{k,\text{turb}}$  can be identified with the turbulent kinetic energy density, although in the rest of the paper we will show them separately. In particular,  $\varepsilon_{k,\text{turb}}$  has the appealing property that it is Galilean invariant, while the filtered energy density  $\varepsilon_k$ , the bulk energy density  $\varepsilon_{k,\text{bulk}}$ , and the cross term  $\varepsilon_{k,\text{cross}}$  depend in general on the choice of frame of reference (see Appendix C.1 for the derivation).

Similarly to the magnetic case, we also define the corresponding filtered energies by volume integrating Eq. (20):

$$\mathcal{E}_k = \mathcal{E}_{k,\text{bulk}} + \mathcal{E}_{k,\text{cross}} + \mathcal{E}_{k,\text{turb}}. \quad (24)$$

In the subsonic limit ( $\mathcal{M} \ll 1$ ), it can be shown that the ratio of the turbulent density fluctuations to the smooth density field is of the order of the Mach number  $\delta\rho_\ell/\langle\rho\rangle_\ell \sim O(\mathcal{M}) \ll 1$  (Appendix C.2); as a result, the transport term  $\varepsilon_{k,\text{cross}}$  and the third-order moment in  $\varepsilon_{k,\text{turb}}$  are asymptotically small and the turbulent kinetic energy density reduces to  $\sum_i \langle \rho \rangle_\ell \mu_2(u_i, u_i)/2$ , which has the same form as the turbulent magnetic energy density (see Appendix C.2 for the derivation). When velocities exceed the sound speed, shocks and discontinuities can form in the flow, i.e., surfaces where one or more fluid variables are discontinuous. From the point of view of smoothing filters, these are thin surfaces (in numerical simulations their thickness is of the order of the cell size, while in reality it may shrink to the scale of several ion skin depths at these collisionless shocks in galaxy clusters), so in general these would also contribute to “turbulence” in the filtered energies. More specifically, from the definitions in Eq. (22)–(23), contact discontinuities where only the density is discontinuous (but with a uniform velocity field) do not contribute to the turbulent kinetic energy density, since the statistical moments vanish if any one of their arguments is spatially constant, but tangential discontinuities (with a non-zero velocity shear) and shocks do. From a physical perspective, it may appear odd that these spatially extended structures can directly contribute to the turbulent energy budget, while one might rather see them as potential sites for the excitation of turbulence (e.g., a shear layer going Kelvin–Helmholtz unstable). We believe that this is more of a conceptual wrinkle, instead of a weakness of the filtering approach, in the same way that shocks affect all of the power spectrum of supersonic turbulence. Having said that, it might still be useful in certain cases to exclude shocks when filtering (as in, e.g., Vazza et al. 2012), although in the present work we do not pursue this approach further.

### 3.3. Example of bulk and turbulent energy densities

In this section, we show a practical application of the filtering method to compute the bulk and turbulent energy densities, shown in Fig. 2. We use the same snapshot as in Fig. 1 with the same filter length  $\ell = 30$  kpc ( $\lambda_c \simeq 160$  kpc), this time displaying both clusters as they are rapidly approaching, with two strong shocks in between. The physical velocities are now computed with respect to the center of mass of the system (only the bulk and cross kinetic energy densities are affected by the shift of frame of reference, see Appendix C.1). A great deal of information can be extracted from the plot: the local three-dimensional velocity  $\sigma_{3D,u}$  and magnetic field dispersion  $\sigma_{3D,B}$  below 160 kpc, which we compute through the second-order moment  $\mu_2$  as

$$\sigma_{3D,u}^2 = \sum_{i=x,y,z} \mu_2(u_i, u_i), \quad \text{and} \quad \sigma_{3D,B}^2 = \sum_{i=x,y,z} \mu_2(B_i, B_i), \quad (25)$$

confirm the impression from Fig. 1 of a relatively quiescent core with higher levels of kinetic turbulence at the virial radius, while the magnetic dispersion decreases with radius throughout. However this picture is partly modified when looking at the kinetic energy densities, which include the contribution of the smooth and turbulent density field: both bulk and turbulent kinetic energy densities, in fact, peak near the cores of the two clusters, where the gas density is much higher, with the turbulent component ( $\varepsilon_{k,\text{turb}}$ ) subdominant but better correlated with the magnetic dispersion, which is expected if the turbulent magnetic and kinetic energies are in equipartition. The cross kinetic energy term ( $\varepsilon_{k,\text{cross}}$ ) is dominated by the turbulent momentum along the merger axis, and is concentrated in the core regions and at large-scale features like shocks.

### 3.4. Physical meaning of the filtered energies

In the previous sections, we introduced the filtered energy densities for the magnetic and kinetic energies. From a mathematical point of view, their definitions follow directly from the second- and third-order statistical moments of the density, magnetic and velocity field. In this section, we briefly discuss some aspects related to their physical interpretation. The reader interested in a practical application may want to jump ahead to Section 4, where we apply the filtering approach to simulations of a major cluster merger. Here we address in particular two questions: (a) how to recover the total energy with the filtering approach, and (b) the connection between the filtered turbulent energy and the power spectrum.

#### 3.4.1. Recovering the total energies

We come back to an apparent inconsistency in the definition of the filtered energy densities (both magnetic and kinetic), that is the fact that for filtered magnetic and kinetic energy densities, Eqs. (12) and (20), (we focus on the magnetic energy, reported below for convenience),

$$\mathcal{E}_B = \varepsilon_{B,\text{bulk}} + \varepsilon_{B,\text{turb}}, \quad (26)$$

the quantity on the left-hand side is technically not the energy density of the total magnetic field  $e_B = \mathbf{B}^2/8\pi$ , but only its filtered counterpart  $\varepsilon_B = \langle e_B \rangle_\ell \neq e_B$ . In other words, it would seem that the filtering approach does not allow us to tally the entirety of the magnetic energy density and recover it as the sum of the smooth and turbulent components.

This apparent limitation is overcome when one considers the volume-integrated energies, Eq. (15), rather than the energy densities. In fact, it is straightforward to show that in an infinite volume or a periodic box the total filtered energy  $\mathcal{E}_B$  is equal to the energy of the total field  $\mathcal{E}_B = E_B$  (see Appendix B). This identity also holds exactly in non-periodic volumes  $V$  when the smoothing kernel is symmetric in its arguments but spatially-varying so that it is normalized over  $V$  without straying beyond its boundaries. For our case where the smoothing kernel is a function of  $|\mathbf{x} - \mathbf{x}'|$  only (which is computationally simpler to implement), a thin buffer region  $\delta V$  of thickness  $\sim \ell$  must be included in the integration in order to correctly normalize  $\mathcal{W}_\ell$ . In this scenario, the total filtered energy  $\mathcal{E}_B$  is found to be approximately equal to the energy of the total field, with an error scaling as  $\mathcal{E}_B - E_B \sim O(\delta V/V)$ , see Appendix B.

To summarize, when the filtered energy densities are integrated over the volume (either periodic or not) we recover the energy of the total field (either exactly or approximately), which

Filtered energy densities before merger  
 $z = 0.51, t = 8.51$  Gyr,  $\ell = 30$  kpc,  $\lambda_c = 158$  kpc

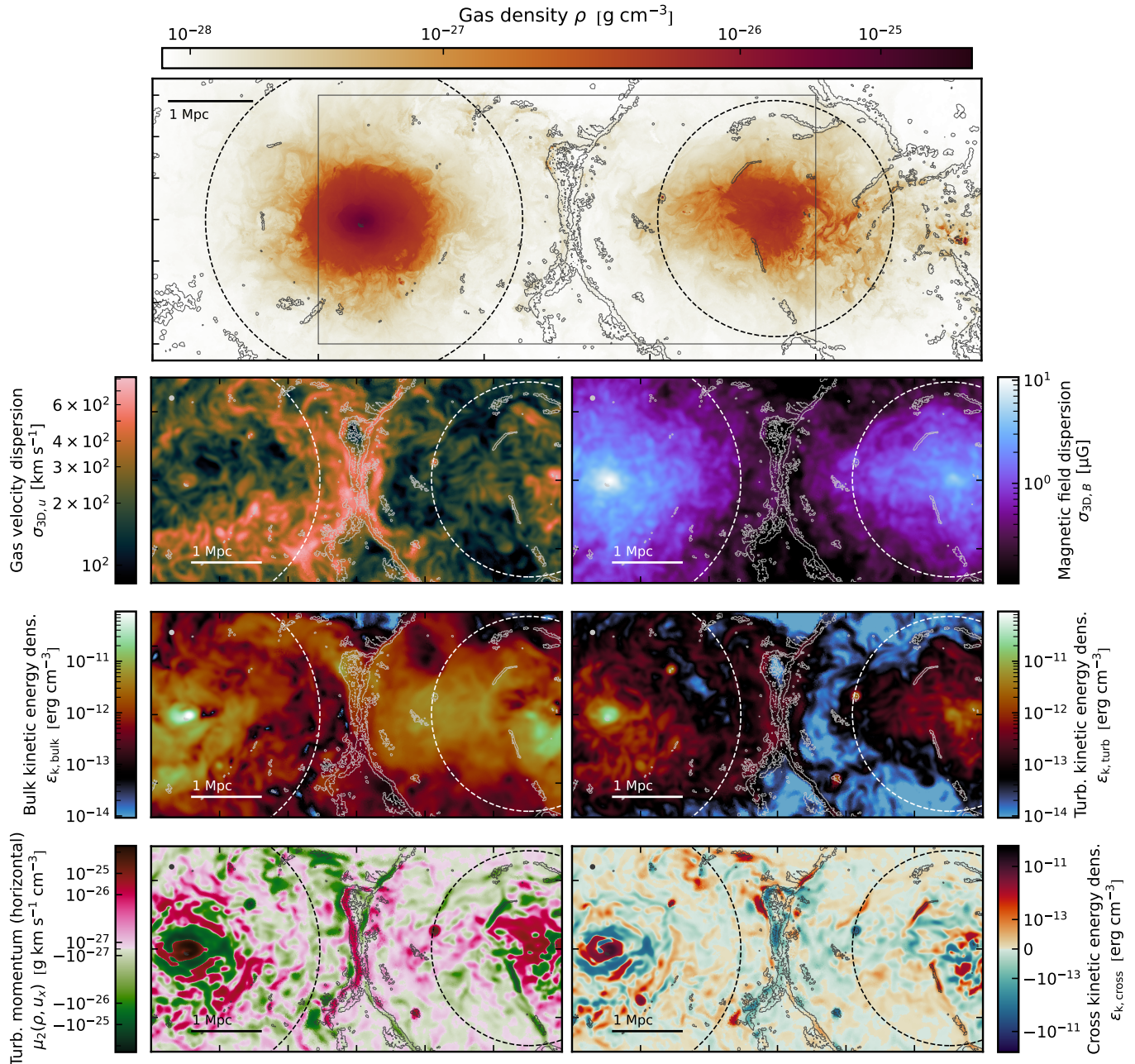


Fig. 2: Filtered energy densities of the merging clusters for a filter scale of  $\ell = 30$  kpc (represented by a beam of radius  $\ell$  in the top left corner). From top to bottom: total density field; kinetic (left) and magnetic (right) turbulent dispersion; bulk (left) and turbulent (right) kinetic energy densities; turbulent momentum along merger axis (left) and cross kinetic energy density (right). Dashed circles are drawn at  $R_{200,c}$  of the two halos, while the contours represent the projected shock surfaces. Velocities are computed with respect to the center of mass of the two clusters. The velocity dispersion is larger in the periphery than in the core, while both the magnetic field dispersion and turbulent kinetic energy peak near the center and far from merger shocks.

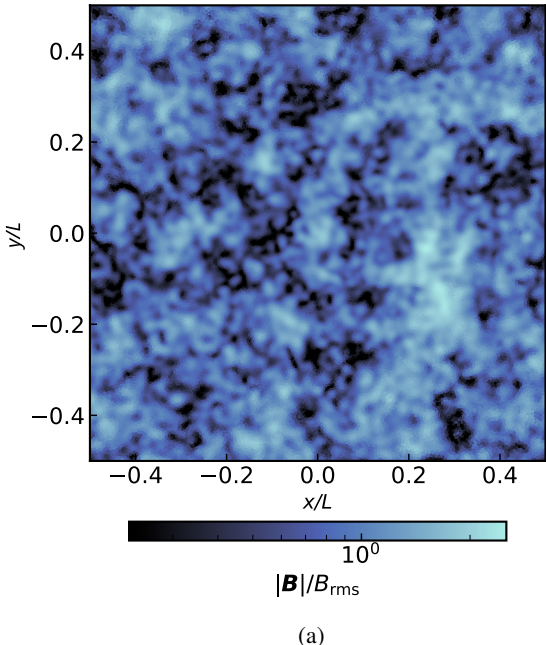
is then correctly partitioned in its entirety between bulk and turbulence.

#### 3.4.2. Turbulent energy and power spectrum

We now focus on the terms that in Eqs. (12) and (20) were identified with the turbulent energies and make explicit their relation-

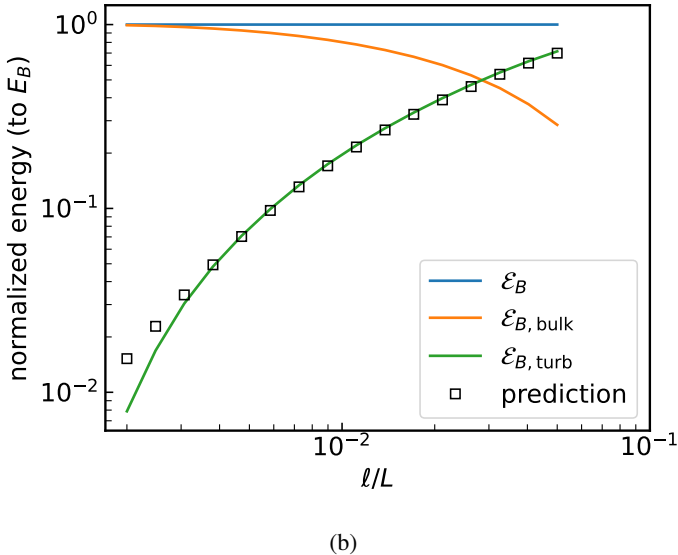
ship with the power spectrum. For illustration, we focus again on the turbulent magnetic energy  $\mathcal{E}_{B,\text{turb}}$ , which involves a second-order statistical moment, but we discuss the case of the turbulent kinetic energy towards the end of the section. We consider here the case of a periodic domain  $V$ . For a discussion on non-periodic volumes (or sub-volumes of a larger periodic domain) see Appendix E.

## Synthetic magnetic field



(a)

## Filtered magnetic energy



(b)

Fig. 3: Decomposition of the magnetic energy according to Eq. (12) as a function of the filtering length  $\ell$  after integrating over the volume. Top: two-dimensional slice of a three-dimensional Kolmogorov synthetic magnetic field. Bottom: the blue line is the filtered total energy of the synthetic turbulent field, the orange line is the energy of the smooth component, while the green is the energy of the turbulent field. The black squares show the analytical result of Eq. (32) obtained by applying the Gaussian filter with scale  $\ell$  to the Fourier components of the synthetic field, and computing the energy of the modes.

We expand the magnetic field in Fourier series as

$$\mathbf{B}(\mathbf{x}) = \sum_{\mathbf{k}} \hat{\mathbf{B}}_{\mathbf{k}} e^{i\mathbf{k} \cdot \mathbf{x}}, \quad (27)$$

where the divergence-free condition for the magnetic field implies non-radial Fourier coefficients  $\hat{\mathbf{B}}_{\mathbf{k}}$ , i.e.  $\mathbf{k} \cdot \hat{\mathbf{B}}_{\mathbf{k}} = 0, \forall \mathbf{k}$ . Con-

volving Eq. (27) with a smoothing kernel  $\mathcal{W}_{\ell}$  using the convolution theorem (Eq. A.9) we obtain the smooth field  $\langle \mathbf{B} \rangle_{\ell}$

$$\langle \mathbf{B} \rangle_{\ell} = V \sum_{\mathbf{k}} \hat{\mathbf{B}}_{\mathbf{k}} e^{i\mathbf{k} \cdot \mathbf{x}} \hat{\mathcal{W}}_{\ell,\mathbf{k}}, \quad (28)$$

where  $\hat{\mathcal{W}}_{\ell,\mathbf{k}}$  is the Fourier transform of the smoothing kernel and satisfies (see Appendix A)

$$\hat{\mathcal{W}}_{\ell,0} = 1/V, \quad \lim_{k\ell \rightarrow \infty} \hat{\mathcal{W}}_{\ell,\mathbf{k}} = 0. \quad (29)$$

For convenience we absorb the factor of  $V$  and define  $\tilde{\mathcal{W}}_{\ell,\mathbf{k}} = V \times \hat{\mathcal{W}}_{\ell,\mathbf{k}}$ . To derive the turbulent energy density  $\varepsilon_{B,\text{turb}}$  we use its definition in Eq. (12), for which we need to compute  $\langle B^2 \rangle_{\ell}$  and  $\langle \mathbf{B} \rangle_{\ell}^2$ . Using the expansion in Fourier series (Eq. 27), the first term can be written as:

$$\begin{aligned} \langle B^2 \rangle_{\ell} &= \left\langle \sum_{\mathbf{k}} |\hat{\mathbf{B}}_{\mathbf{k}}|^2 + \sum_{\mathbf{k} \neq \mathbf{k}'} \hat{\mathbf{B}}_{\mathbf{k}}^* \cdot \hat{\mathbf{B}}_{\mathbf{k}'} e^{i(\mathbf{k}' - \mathbf{k}) \cdot \mathbf{x}} \right\rangle_{\ell} \\ &= \sum_{\mathbf{k}} |\hat{\mathbf{B}}_{\mathbf{k}}|^2 + \sum_{\mathbf{k} \neq \mathbf{k}'} \hat{\mathbf{B}}_{\mathbf{k}}^* \cdot \hat{\mathbf{B}}_{\mathbf{k}'} e^{i(\mathbf{k}' - \mathbf{k}) \cdot \mathbf{x}} \tilde{\mathcal{W}}_{\ell,\mathbf{k}' - \mathbf{k}}, \end{aligned} \quad (30)$$

where we applied again the convolution theorem (Eq. A.9) to filter a sum of plane waves, in which each wave is filtered by multiplying it by  $\tilde{\mathcal{W}}_{\ell,\mathbf{k}' - \mathbf{k}}$ . Taking now the square of Eq. (28) and subtracting it from Eq. (30), we obtain the turbulent energy density of the magnetic field at every point in space:

$$\begin{aligned} 8\pi \varepsilon_{B,\text{turb}}(\mathbf{x}) &= \sum_{\mathbf{k}} |\hat{\mathbf{B}}_{\mathbf{k}}|^2 (1 - |\tilde{\mathcal{W}}_{\ell,\mathbf{k}}|^2) \\ &+ \sum_{\mathbf{k} \neq \mathbf{k}'} \hat{\mathbf{B}}_{\mathbf{k}}^* \cdot \hat{\mathbf{B}}_{\mathbf{k}'} e^{i(\mathbf{k}' - \mathbf{k}) \cdot \mathbf{x}} [\tilde{\mathcal{W}}_{\ell,\mathbf{k}' - \mathbf{k}} - \tilde{\mathcal{W}}_{\ell,\mathbf{k}} \tilde{\mathcal{W}}_{\ell,\mathbf{k}' - \mathbf{k}}]. \end{aligned} \quad (31)$$

Equation (31) consists of a constant term (the first), and spatially-varying term (the second). The constant term is a weighted sum of the energy in different Fourier modes, while the spatially-varying cross term represents the interference between different wave vectors  $\mathbf{k} \neq \mathbf{k}'$ . Since the spatially-varying term is a sum of complex exponentials, it vanishes exactly when integrated over the entire periodic volume  $V$ . Thus, after integration we are left with

$$\varepsilon_{B,\text{turb}} = \sum_{\mathbf{k}} \frac{|\hat{\mathbf{B}}_{\mathbf{k}}|^2}{8\pi} (1 - |\tilde{\mathcal{W}}_{\ell,\mathbf{k}}|^2) V. \quad (32)$$

For any kernel  $\tilde{\mathcal{W}}_{\ell,\mathbf{k}}$  decaying sufficiently fast when  $k\ell > 1$ , this can be approximated as

$$\varepsilon_{B,\text{turb}} \approx \sum_{k\ell > 1} \frac{|\hat{\mathbf{B}}_{\mathbf{k}}|^2}{8\pi} V, \quad (33)$$

which is the amount of energy present on scales smaller than the filter size  $\ell$ . Conversely, the energy of the smooth magnetic field is the amount of energy present on scales greater than  $\ell$  ( $k\ell < 1$ ). This result clarifies the specific sense in which we identify  $\varepsilon_{B,\text{turb}}$  with the “turbulent” magnetic energy, i.e. this is the energy contained in the scales smaller than the filter size. A similar argument applies to the turbulent kinetic energy in the subsonic regime, where it can be shown that the largest contribution to the turbulent kinetic energy is

$$\mathcal{E}_{k,\text{turb}} + \mathcal{E}_{k,\text{cross}} \approx \frac{1}{2} \rho_0 \sum_{k\ell > 1} |\hat{\mathbf{u}}_{\mathbf{k}}|^2 V, \quad (34)$$

where  $\rho_0$  is the mean density in the volume. The same expression with the sum running over  $k\ell < 1$  gives instead the bulk kinetic energy  $\mathcal{E}_{\text{bulk}}$ . In the weakly compressible/transonic regime the full expression of the turbulent kinetic energy is algebraically involved, as it now includes triad interactions between the density and the velocity field. Contributions from wavenumbers that are all large-scales ( $k\ell \ll 1$ ) are still filtered out, but interactions between mixed wavenumbers are in general unavoidable. A similar situation arises when computing the spectral kinetic energy density in compressible turbulence (e.g., Kida & Orszag 1990; Grete et al. 2017).

We use Eq. (32) to numerically verify our algorithm. We initialize a synthetic turbulent magnetic field that follows a Kolmogorov spectral density energy,  $E(k) \propto k^{-5/3}$  on a non-uniform three-dimensional Voronoi mesh (Fig. 3a). We then compute the total, bulk and turbulent filtered energy densities using a Gaussian kernel for different filter sizes  $\ell$ , and integrate them over the periodic volume. The resulting filtered energies are shown in Fig. 3b, together with the analytical prediction from the power spectrum of the fluctuations (Eq. 32). The two measures agree very well, except for small  $\ell$ , where the finite resolution of the mesh plays a role. We note that, by construction, with a Gaussian kernel the turbulent energy (bulk energy) monotonically increases (decreases) with the filter size  $\ell$ , as more of the Fourier modes get progressively classified as “turbulence”. This is not necessarily the case if the Fourier amplitude of the kernel is not monotonic (as with the spherical top-hat, see Appendix A). In the case of the kinetic energy, even with a monotonic kernel, it is not possible to predict a priori the behavior of the turbulent and bulk energies with  $\ell$  because the contribution from triad interactions of small- and large-scale wave vectors can be either positive or negative. If the flow is highly subsonic, then the same considerations outlined above for the magnetic energy apply.

### 3.5. Connection with LES

Smoothing filters have long been used in turbulence theory to simultaneously resolve physical processes in both space and scale (Leonard 1974; Rogallo & Moin 1984; Lesieur & Metais 1996; Meneveau & Katz 2000), without placing restricting assumptions on scale separation in the flow. They are at the core of large-eddy simulation methods (LES), where the Navier-Stokes equations (or MHD, as in, e.g., Grete et al. 2015) are filtered (“coarse-grained”) and simulated without the need to resolve the small Kolmogorov dissipation scale directly. As is well known, the downside is the appearance of an additional term in the momentum equation that represents stresses below the grid scale that needs to be modeled (see discussion in Schmidt 2015, for applications of LES methods in astrophysics). This stress tensor is in fact mathematically the same as the second-order statistical moment  $\mu_2(u_i, u_j)$  in Eq. 10, and similarly the Maxwell subgrid-scale stress tensor can be written in terms of  $\mu_2(B_i, B_j)$ .

In this work, we are less interested in the modeling of subgrid-scale stresses than in applying the same filtering machinery to study the contribution of different processes at the scales of choice. In particular, the filtering approach allows us to define notions of large-scale and small-scale energies, for which it is possible to write down rigorous equations for their time evolution. One complication in compressible turbulence arises from the fact that filtered fields and energies are not uniquely defined (see, e.g., Aluie 2013). For instance, one may define the large-scale momentum as either  $\langle \rho \mathbf{u} \rangle_\ell$  or  $\langle \rho \rangle_\ell \langle \mathbf{u} \rangle_\ell$ . Certain choices are favored based on physical considerations, e.g. the

Galilean invariance of terms such as the subgrid-scale stress tensor (Appendix C.1).

In this work we follow Hollin’s choice (Hollins et al. 2022) which is based on the decomposition of the bulk kinetic energy density of compressible flows by Monin & Yaglom (1971, Sec. 6.4), replacing Reynolds averaging with filter averaging. This choice allows for simple and physically transparent interpretation of the bulk, turbulent and cross/transport terms of the kinetic energy, as outlined in Sec. 3.2. Another popular option for compressible flows is to weigh all functions by the fluid density before averaging, also known as Favre averaging (Favre 1983). For example, in this approach the Favre-filtered velocity is  $\tilde{\mathbf{u}}_\ell \equiv \langle \rho \mathbf{u} \rangle_\ell / \langle \rho \rangle_\ell$ , as opposed to simply  $\langle \mathbf{u} \rangle_\ell$ . In the subsonic limit, the two averages coincide. The advantage of Favre averaging is that it satisfies a so-called “inviscid criterion”, i.e. it guarantees that viscous contributions are negligible when  $\ell$  is larger than the viscous scale (Aluie 2013). This property was used to show that kinetic energy cascades locally also in compressible turbulence (Aluie 2011; Wang et al. 2013). For our purposes, the simpler definitions of filtered quantities by Monin & Yaglom (1971) suffice. However, if one is interested in looking at the energy flux across scales (which we plan to do in future work), Favre averaging might represent a better choice.

## 4. Turbulent energies during a cluster merger

### 4.1. PICO-Clusters simulations

We now apply the methods outlined in the previous sections to a simulation of a massive galaxy cluster ( $M_{200,c} \simeq 2.72 \times 10^{15} \text{ M}_\odot$  at  $z = 0$ ). This cluster, `Hal03`, is part of the PICO-Clusters suite (Berlok et al, in prep.), which re-simulates 24 massive clusters ( $\gtrsim 10^{15} \text{ M}_\odot$ ) from a 1.5 Gpc-wide cosmological volume using the zoom-in technique and the moving-mesh code AREPO (Springel 2010; Pakmor et al. 2016; Weinberger et al. 2020). The AREPO code evolves the comoving form of the ideal MHD equations (Pakmor & Springel 2013), including radiative physics and the effective model of galaxy formation used in the ILLUSTRISTNG simulations (Weinberger et al. 2017; Pillepich et al. 2018). The simulations shown in this paper have been run with a mass resolution for dark-matter particles of  $5.9 \times 10^7 \text{ M}_\odot$  and with a target gas mass of  $7 \times 10^6 \text{ M}_\odot$ , which is comparable to that of the TNG300 cosmological volume simulation (Springel et al. 2018). Further details on the PICO-Clusters suite can be found in Tevlin et al. (2025), and will be outlined extensively in an upcoming publication (Berlok et al, in prep.).

Of the 24 Halos simulated in PICO-Clusters, we choose `Hal03` because it undergoes a major merger at low-redshift with a second massive halo ( $M_{200,c} \simeq 5.38 \times 10^{14} \text{ M}_\odot$ , mass ratio of 2.4 before merger), which generates significant bulk motions and sloshing in the center. For this reason, it represents a good candidate to test our decomposition of bulk and turbulent energies. Moreover, its time evolution was analyzed in detail in Tevlin et al. (2025), allowing us to compare our results directly.

### 4.2. Filtered fields during merger

Similarly to Fig. 1, we show now the total, bulk and turbulent fields during the merger for the intermediate filter length  $\ell = 30 \text{ kpc}$  (see Fig. 4), when the core of the less massive cluster has rammed into the core of `Hal03`. The infalling less massive cluster is especially visible in the density and velocity field, where one can observe strong asymmetric features and the large radial inflow, respectively. The overall level of turbulent density

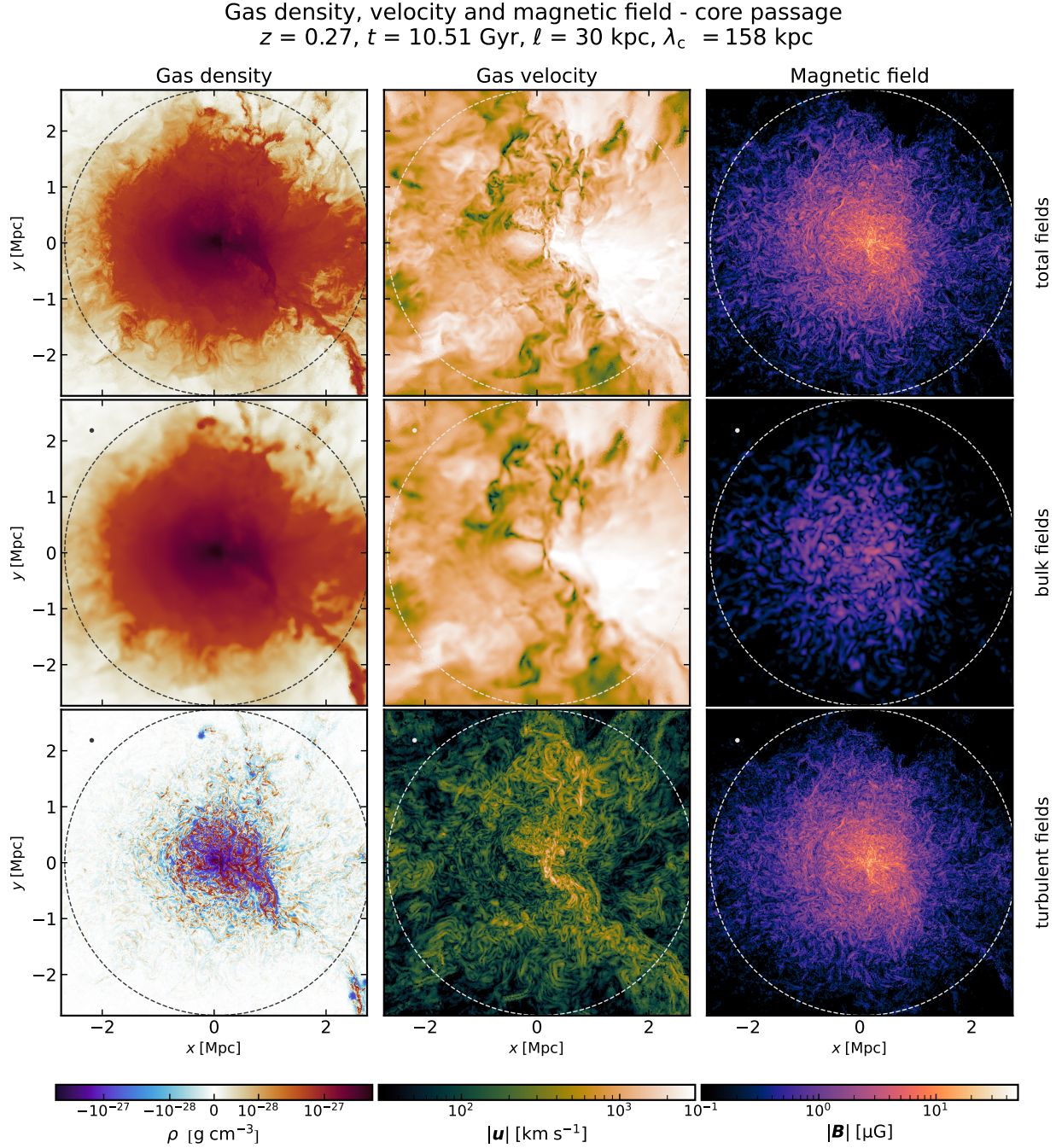


Fig. 4: Decomposition of the density, velocity (in the rest system of the main cluster) and magnetic field of Halo3 during the merger ( $z = 0.27$ ) for a filter scale of 30 kpc (represented by a beam of radius  $\ell$  in the top left corner). The layout of the figure is the same as in Fig. 1. The cluster is highly disturbed by the infall of the less massive companion (along the horizontal axis, from the right side). The infall is accompanied by a large-scale inflow, without however significant small-scale fluctuations. The magnetic field remains more homogeneously distributed throughout the volume.

fluctuations increases and high levels of turbulent velocities are excited along the contact discontinuity. On the contrary, except for a small region in the cluster center showing strong amplification (likely due to adiabatic compression), the turbulent magnetic field appears to be more homogeneously distributed in the entire volume.

#### 4.3. Turbulent and bulk energies

We now apply the definitions of the bulk/turbulent kinetic and magnetic energies of Section 3, and follow their evolution in time throughout the merger starting from  $t = 6$  Gyr until the present time. We use a Gaussian filter with constant-in-physical-space filter length throughout the time-series. To better understand how the energies are partitioned between different scales, we select three different lengths, i.e.,  $\ell = \{15, 30, 59\}$  kpc. In

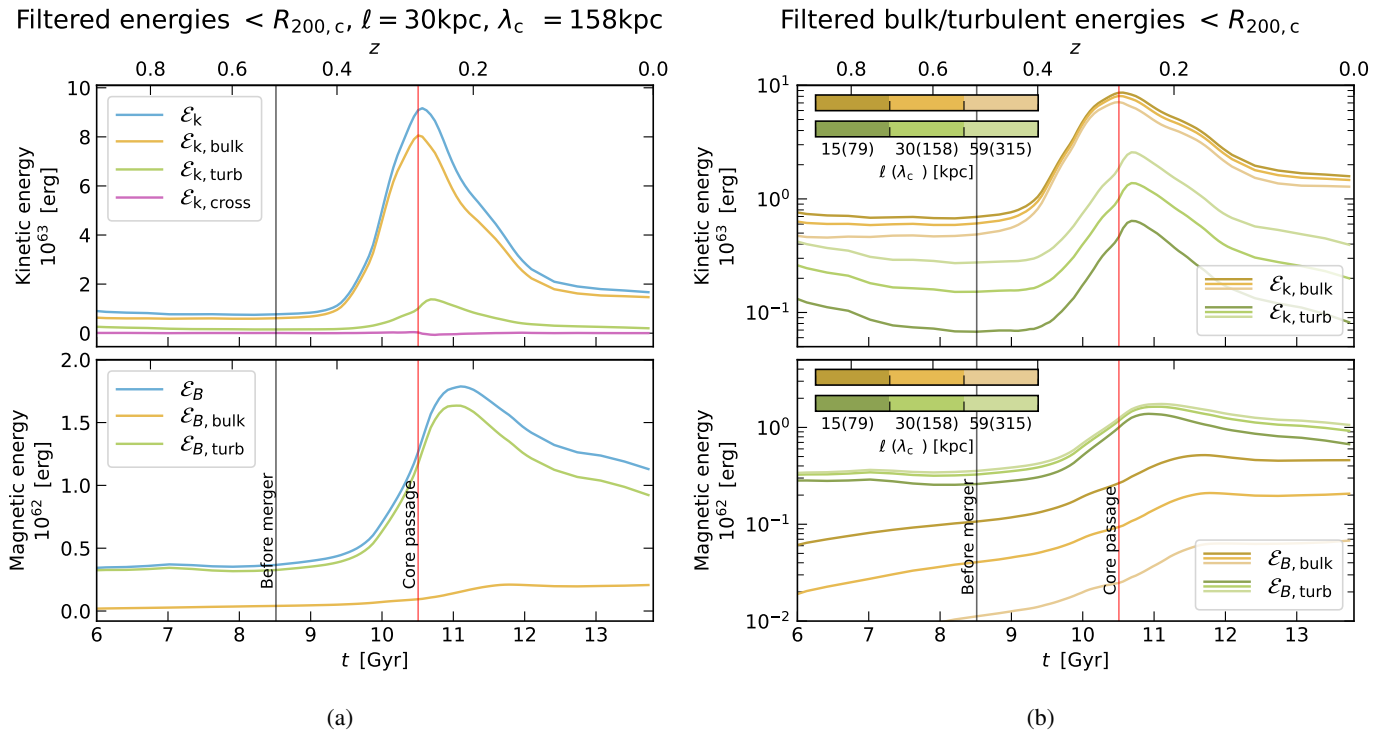


Fig. 5: Time evolution of the filtered kinetic and magnetic energies during the major merger. Left column: kinetic (top) and magnetic energy (bottom) and their decomposition according to Eqs. (15) and (24) for a fiducial filter scale of 30 kpc corresponding to a cutoff wavelength of  $\approx 160$  kpc. The vertical lines correspond to the time of the snapshots shown in Figs. 1 and 4. Right column: bulk and turbulent energies for different filter scales. For the scales considered, the turbulent kinetic energy is always subdominant compared to the bulk throughout the merger, while the reverse is true for the turbulent magnetic energy.

terms of effective physical wavelength ( $\lambda_c$ ) they approximately correspond to 80, 160 and 320 kpc, which amount to 2.7%, 5.4% and 10.8% of  $R_{200,c}$  at  $z = 0$ , respectively. The filtered energy densities are then integrated within  $R_{200,c}$  of *Hal03* to obtain the filtered energies.

We show the results of the decomposition in Fig. 5a for a fiducial filter scale  $\ell = 30$  kpc ( $\lambda_c \approx 160$  kpc). Several features can be observed. The kinetic and magnetic energies differ in that most of the kinetic energy resides in the bulk flow rather than the turbulent component for the interval shown in Fig. 5a, while the reverse is true for the magnetic energy. During the merger, the total, bulk and turbulent kinetic energies increase substantially by roughly a factor of ten between the times of the snapshots in Fig. 1 and Fig. 4, albeit at different rates. The total and the bulk kinetic energies (which also include the overall acceleration of the less massive cluster towards *Hal03*) begin to increase and reach their peak earlier than the turbulent energy, around the time when the cores collide. The transport term is subdominant throughout and reverses sign around the time of the core passage. The magnetic energy is instead amplified by a factor of five, similar for both the bulk and turbulent components. Interestingly, the turbulent magnetic energy reaches its peak slightly delayed with respect to the turbulent kinetic energy ( $\approx 300$  Myr), and decays more slowly afterwards.

We repeat the same calculations for a lower and higher value of the filter scale, corresponding to a cutoff wavelength of about 80 kpc and 320 kpc. The bulk and turbulent components are shown in Fig. 5b. As we increase the filter scale, the turbulent energies (both magnetic and kinetic) increase, while the bulk energies decrease. This is a consequence of the fact that, as we increase  $\ell$ , more and more modes are classified by the smooth-

ing filter as ‘‘turbulence’’, and consequently fewer of them as ‘‘bulk’’. This trend is strictly monotonic for the magnetic energy, while this is not guaranteed in principle for the kinetic energy due to the presence of the cross term: while in our case it is subdominant, in strongly asymmetric configurations it could become highly negative (this is the case of outflows from galactic disks; Hollins et al. 2022). Whereas the overall behavior of the bulk and turbulent energies for the different filter scale reflects that of Fig. 5a, the change in the energy levels with respect to  $\ell$  provides us with more information on how energy is partitioned across different scales. For instance, in the case of the kinetic energy doubling or halving the filter scale boosts the turbulent energy by roughly the same factor, whereas for the magnetic energy there is relatively little difference between the turbulent levels for the different filter scales. This suggests that, for this range of scales, the kinetic energy increases with  $\ell$  following a power law, while the magnetic field is predominantly tangled on scales below 80 kpc. After the merger, both kinetic and magnetic turbulent energies decay faster the smaller the filter scale, which is to be expected for viscous and resistive numerical dissipation as we approach the grid scale.

To compare the levels of turbulence detected with the filtering approach with other methods and with observations, we compute the turbulent kinetic,  $f_{k,\text{turb}}$ , and magnetic pressure fraction,  $f_{B,\text{turb}}$ , within  $R_{200,c}$  and for the different filter scales. In the filtering approach, we define them as:

$$f_{k,\text{turb}} \equiv \frac{\mathcal{E}_{k,\text{turb}}}{\mathcal{E}_{k,\text{turb}} + E_{\text{th}}}, \quad f_{B,\text{turb}} \equiv \frac{\mathcal{E}_{B,\text{turb}}}{\mathcal{E}_{k,\text{turb}} + \mathcal{E}_{B,\text{turb}} + E_{\text{th}}}, \quad (35)$$

where the dependence on the filter scale  $\ell$  is implicit in the definition of the turbulent energies  $\mathcal{E}_{k,\text{turb}}$  and  $\mathcal{E}_{B,\text{turb}}$ . Note that the

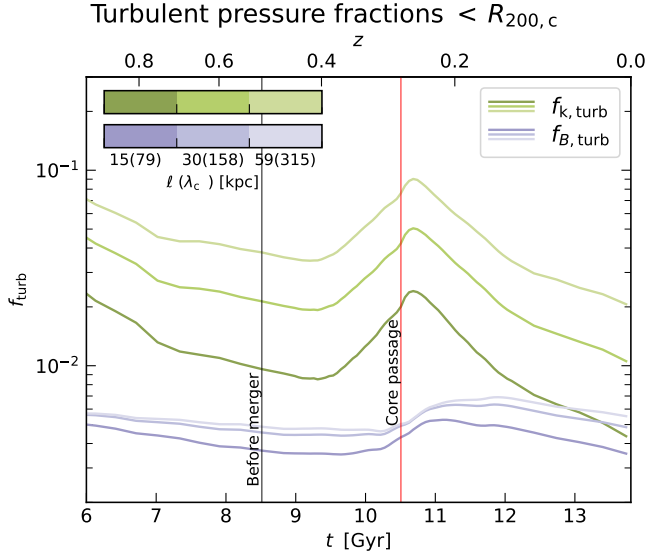


Fig. 6: Time evolution of the kinetic and magnetic turbulent pressure fraction during a major merger for different filter lengths. The turbulent kinetic pressure decreases to pre-merger levels within 1 – 1.5 Gyr from the core passage.

different normalization in the denominator was chosen to allow direct comparison of  $f_{k,\text{turb}}$  with the non-thermal pressure fraction  $f_{\text{nth}}$ , which is commonly reported in the context of XRISM and observational studies, and where contributions from magnetic fields and other non-thermal source of pressure are usually neglected<sup>2</sup> (Eckert et al. 2019). It is useful to recast the kinetic pressure fraction in terms of the mean turbulent pressure  $p_{\text{turb}}$  below a scale  $\ell$ , and mean thermal pressure  $p_{\text{th}}$  in a volume  $V$ , where

$$p_{\text{turb}} \equiv \frac{2}{3} \frac{\mathcal{E}_{k,\text{turb}}}{V}, \quad (36)$$

and the thermal pressure is related to the thermal energy by the usual relation  $p_{\text{th}} = (\gamma - 1)E_{\text{th}}/V$ . Our definition<sup>3</sup> of the turbulent/non-thermal pressure (Eq. 36) is consistent with, but not identical to that routinely employed in observational studies using the line-of-sight velocity dispersion  $\sigma_{\text{los}}$ , ( $p_{\text{turb}} \simeq \rho_0 \sigma_{\text{los}}^2$  Eckert et al. 2019), where a homogeneous medium with gas density  $\rho_0$  and isotropic turbulence is assumed. Equation (36), instead, is constructed through the filtered turbulent kinetic energy  $\mathcal{E}_{k,\text{turb}}$  (Eqs. 23–24), which depends on the filter scale  $\ell$ . By taking the same limit of subsonic, homogeneous and isotropic turbulence, we show in Appendix C.3 that the turbulent pressure in Eq. (36) reduces to  $p_{\text{turb}} \simeq \rho_0 \sigma_{1D,u}^2$ , where  $\sigma_{1D,u}^2 = \sigma_{3D,u}^2/3$  is the isotropic one-dimensional velocity dispersion (here it represents an rms value over the volume  $V$ ). Replacing  $\sigma_{1D,u}$  with  $\sigma_{\text{los}}$ , we can see that the two formulations are indeed analogous.

Using Eq. (36) and assuming an adiabatic index of  $\gamma = 5/3$ , the turbulent kinetic pressure fraction can be expressed as

$$f_{k,\text{turb}} = \frac{p_{\text{turb}}}{p_{\text{turb}} + p_{\text{th}}}, \quad (37)$$

<sup>2</sup> For typical ICM conditions the contributions of magnetic field (Carilli & Taylor 2002; Tevlin et al. 2025) and cosmic ray pressure are each less than  $\approx 1\%$  (Ackermann et al. 2010, 2014; Ruszkowski & Pfrommer 2023).

<sup>3</sup> A similar expression was already introduced in the context of smoothing filters (Wang & He 2024a), although ours is more general since it does not place assumptions on subsonic or isotropic turbulence.

which can be further simplified if we again assume subsonic, homogeneous turbulence (see Appendix C.3): we first introduce the corresponding three-dimensional  $\mathcal{M}_{3D}$  and one-dimensional turbulent Mach number  $\mathcal{M}_{1D}$ ,

$$\mathcal{M}_{3D}^2 \equiv \frac{\sigma_{3D,u}^2}{c_s^2}, \quad \text{and} \quad \mathcal{M}_{1D}^2 \equiv \frac{\sigma_{1D,u}^2}{c_s^2}, \quad (38)$$

and after substituting in Eq. (36), the turbulent kinetic pressure fraction becomes:

$$f_{k,\text{turb}} \simeq \frac{\sigma_{3D,u}^2}{\sigma_{3D,u}^2 + \frac{3k_B T}{\mu m_u}} = \frac{\mathcal{M}_{3D}^2}{\mathcal{M}_{3D}^2 + \frac{3}{\gamma}} \quad (39)$$

$$= \frac{\mathcal{M}_{1D}^2}{\mathcal{M}_{1D}^2 + \frac{1}{\gamma}} \quad (\text{for isotropic turbulence}), \quad (40)$$

where we used that  $c_s^2 = \gamma k_B T / (\mu m_u)$ , with  $T$  the mean temperature,  $k_B$  is the Boltzmann constant,  $\mu$  the mean molecular weight, and  $m_u$  the atomic mass unit. Equations (39)–(4.3) are formally analogous to the non-thermal pressure fractions routinely used in observational studies of galaxy clusters (e.g., Eq. 10 of Eckert et al. 2019), or by the XRISM Collaboration (Eq. 1 of both XRISM Collaboration et al. 2025a,b).

After introducing the necessary quantities, we show in Fig. 6 the evolution of the turbulent kinetic and magnetic pressure fraction during the major merger for the three filter lengths considered. We notice a similar trend for the turbulent kinetic pressure with all filter lengths, with a sharp exponential-like increase during the merger that peaks near the core passage; the subsequent relaxation takes place in two phases: a first rapid decrease, followed by a slower decline. A similar dual trend was also observed in earlier work by Shi et al. (2018), where it was attributed to faster decay of turbulence in the inner regions of the cluster. For the intermediate filter length  $\ell = 30$  kpc ( $\lambda_c \simeq 160$  kpc), we measure a maximum kinetic turbulent fraction of  $f_{k,\text{turb}} \simeq 5\%$  near the core passage at  $t \simeq 10.7$  Gyr ( $z \simeq 0.26$ ), followed by a rapid decay to 2% by  $t = 12$  Gyr, and to 1% by the present time. For larger filter scales these numbers tend to increase, but even for our largest scale probed,  $\ell \simeq 60$  kpc ( $\lambda_c \simeq 320$  kpc), where  $f_{k,\text{turb}} \simeq 9\%$  during the core passage, the kinetic turbulent fraction quickly decreases to  $\simeq 3.5\%$  by  $t = 12$  Gyr, and to only 2% by the present time. We stress that these estimates refer to the entire cluster within  $R_{200,c}$ , and that the values may be different if we restrict ourselves to only the central region due to AGN feedback (we defer such an analysis with a more detailed comparison to XRISM data to future studies).

Similar to the results shown in Fig. 5, the turbulent magnetic pressure fraction is always lower than the corresponding turbulent kinetic pressure, although after the merger it decays much more slowly (e.g., for  $\ell = 30, 60$  kpc,  $f_{B,\text{turb}}$  is still higher than pre-merger levels after  $\gtrsim 3$  Gyr from the core passage). Kinetic turbulent fractions of  $\sim 1 – 2\%$  after relaxation are roughly comparable to those found in Valdarnini (2019), but lower than those in Groth et al. (2025), although multi-scale filtering were employed in both studies. A more direct comparison may be drawn with the massive clusters in Vazza et al. (2011), who also used fixed-scale filters of various sizes (but with a different kernel), and who found turbulent to thermal fractions below 300 kpc of 20% to 40% within  $R_{200,c}$  for relaxed clusters and during major mergers, respectively, which are significantly larger than our estimates.

Our results suggest that, unless a cluster has undergone a major merger within the last 1 – 1.5 Gyr, values of 2 – 3% for the

turbulent kinetic pressure fraction are not unusual, provided one carefully removes large-scale bulk motions. Our values of  $f_{k,\text{turb}}$  are in the same ballpark as the observational estimates from the XRISM cluster sample in the regions farther away from the core (XRISM Collaboration et al. 2025c), where we expect the effect of AGN feedback to be strongest. One caveat is that the estimates of the velocity dispersion with XRISM include all motions along the line-of-sight (LOS), which could in principle be a combination of both bulk motions (e.g., sloshing) and actual small-scale turbulence. Nevertheless, it is possible to associate these measurements of the velocity dispersion with an “effective length”, which measures the size of the region that contributes most to the X-ray flux (XRISM Collaboration et al. 2025e). This effective length provides an upper bound for the physical scales of the velocity fluctuations probed by XRISM, and may be compared to the smoothing length used in the filtering approach. We defer a more in-depth comparison with observations to a future publication.

## 5. Pitfalls of multiscale iterative filters

After showing a practical application of the filtering method at fixed scale, we discuss an alternative approach based on multiscale iterative filters and highlight its potential pitfalls.

### 5.1. Motivation

Given the wide range of processes in the ICM that can excite turbulence, any one value of  $\ell$  for the entire cluster will be inadequate to single out the different scales at which they operate (e.g., in the Perseus cluster two independent drivers of turbulent motions on different scales were identified: due to the AGN feedback in the inner region, and to mergers in the outer core, XRISM Collaboration et al. 2025e). For this reason, only by repeating the operation of filtering and computing the filtered energies for different lengths (as we did in Section 4) can one gain a more complete picture.

To obviate this issue, a popular approach (originally pioneered by Vazza et al. 2012) is to employ an iterative scheme to locally determine the injection scale of the turbulence, and therefore distinguish the bulk from the turbulent component. In this iterative method, a kernel of increasingly larger size  $\ell_n$  is applied to a physical field (e.g., gas density), until a certain convergence criterion is met. Key to this approach is that the final  $\ell_n$  of convergence (identified with the correlation scale of the turbulence) can differ from place to place. For a scalar field  $f(\mathbf{x})$  with decomposition  $f = \langle f \rangle_{\ell_n} + \delta f_{\ell_n}$  the convergence criterion chosen by Vazza et al. (2012) evaluated at the  $n$ -th iteration reads:

$$\left| \frac{\delta f_{\ell_n} - \delta f_{\ell_{n-1}}}{\delta f_{\ell_{n-1}}} \right| \leq \epsilon, \quad (41)$$

where  $\epsilon$  is a small tolerance parameter (typically  $\epsilon = 0.02 - 0.1$ ). For a vector field the procedure is either repeated for the individual components (as originally proposed by Vazza et al. 2012, although this could lead to different components being filtered on disparate scales), or carried out using all components at once (Vazza et al. 2017). The iterative algorithm can optionally be complemented with a shock finder scheme in order to exclude from the averaging regions that are physically separated by a shock front, and that therefore do not communicate with each other (Vazza et al. 2012, 2017). Other variants of the basic multiscale filter have been adopted in the literature, e.g., for use with smoothed-particle hydrodynamics codes (Valdarnini 2019), with

variable tolerance  $\epsilon$  (Angelinelli et al. 2020), or with different convergence criteria (Vallés-Pérez et al. 2021, 2024).

### 5.2. Numerical tests

We implement the iterative multiscale filter in our analysis code following Vazza et al. (2012) and perform a wide range of tests on idealized setups and simulated galaxy clusters. After extensive exploration, we conclude that multiscale iterative filters suffer from certain issues that complicate the interpretation of the results and that render them unsuitable as a one-size-fits-all solution to determine the levels of turbulence in the ICM. These issues stem from the fact that the convergence of the iterative scheme is susceptible to noise and strongly depends on the initial conditions. In what follows, we discuss two representative test scenarios that highlight their pitfalls.

#### 5.2.1. Kelvin–Helmholtz instability

In the first scenario we test the iterative filter against the Kelvin–Helmholtz instability, which is a ubiquitous hydrodynamical instability in the ICM caused, e.g., by ram-pressure stripping in merging galaxies or near sloshing cores (Walker et al. 2017). We set up an inviscid, hydrodynamic version of the simulation setup described in Lecoanet et al. (2016) and Berlok & Pfrommer (2019), and with the same AREPO settings as in Berlok et al. (2020). This is a sub-sonic simulation with a density contrast of two across the shear layer.

We focus on the density field after the instability is well into its nonlinear stage, and compare the iterative multiscale filter to the fixed-scale filter where we choose a fiducial smoothing length  $\ell$ . Both versions use a Gaussian kernel, which has better convergence properties than the spherical top-hat (see Appendix A for a comparison). The results are shown in Fig. 7. By looking at the top and bottom panels, we observe significant differences between the two filters: in the unperturbed region of the flow, the iterative filter did not correctly subtract the smooth field from the turbulent component, thus returning a non-zero turbulent field; conversely, near the mixing layer of the Kelvin–Helmholtz rolls, the smooth field obtained with the iterative filter contains spurious small structures that are not present with the fixed-scale filter.

We attribute this behavior to the fact that neighboring cells have iteratively converged to very different filter lengths, as can be seen from the lower left panel. In particular, the criterion in Eq. (41) is ill-conditioned when the fluctuating density field is close to zero, because  $\delta\rho_\ell$  appears in the denominator. For example, as we increase  $\ell$ , in the unperturbed part of the flow  $\rho$  is approximately constant and  $\delta\rho_\ell = \rho - \langle \rho \rangle_\ell$  can be arbitrarily small (e.g., up to floating point precision errors due to the numerical integration). Consequently, even small changes between successive iterations may exceed the tolerance threshold  $\epsilon$  and the iteration will not converge, leading to contamination of the local value of  $\delta\rho_\ell$  by regions very far away. This is visible, e.g., in the bottom-left corner of Fig. 7, where numerical artifacts (striations) are present in the smooth and turbulent fields.

#### 5.2.2. Double-bump

The second scenario examines the performance of the iterative filter in the presence of fluctuations that live on two sets of scales that are widely separated in wavenumber space. This test should be thought of as an idealized version of what may happen when

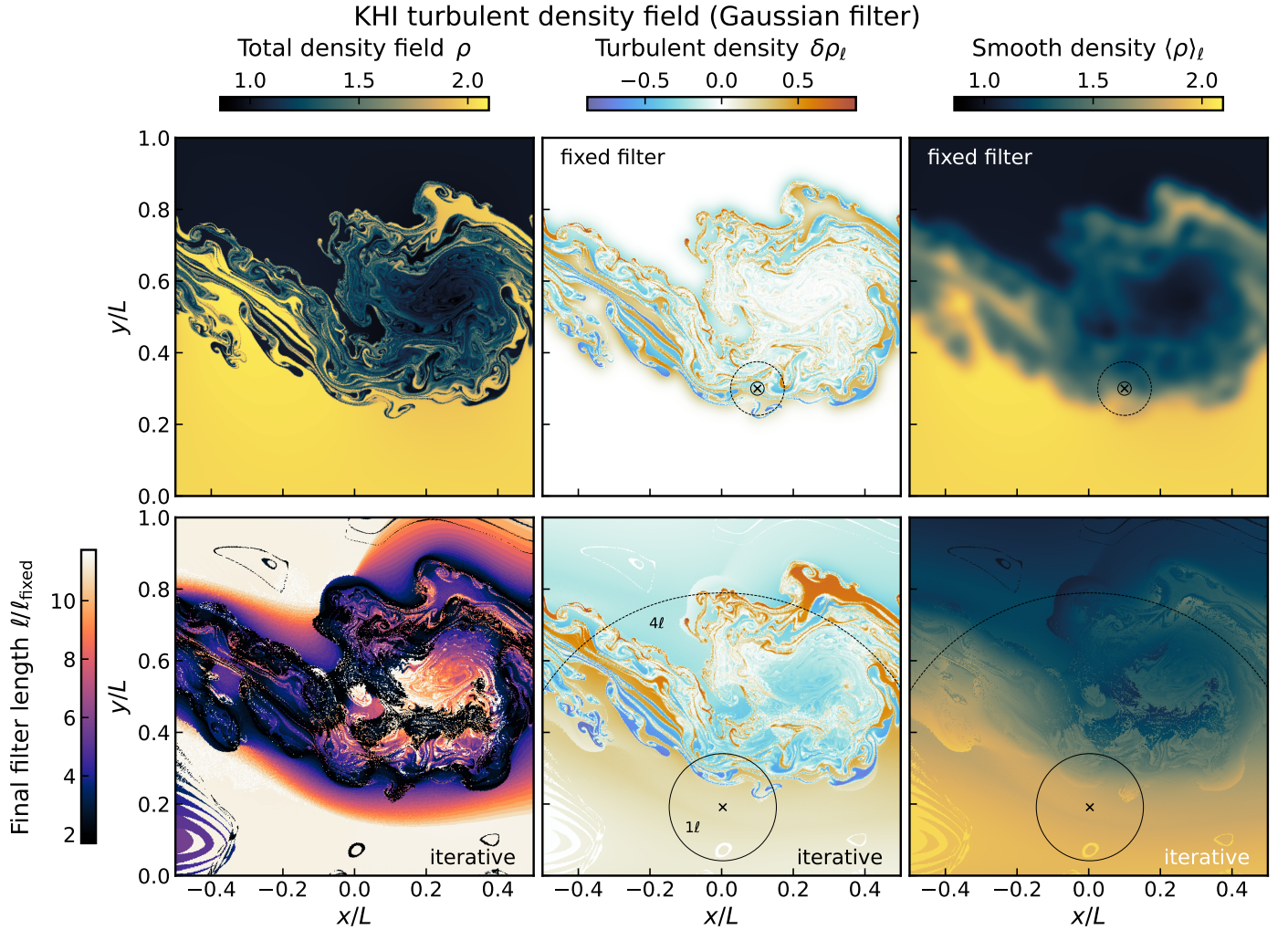


Fig. 7: Comparison between iterative multiscale filter (tolerance  $\epsilon = 0.05$ ) and fixed-scale filter using a Gaussian kernel with a two-dimensional simulation of a Kelvin–Helmholtz instability run with AREPO (only the upper half of the domain is shown). In the second and third columns, the top (bottom) panel shows the result of fixed scale (iterative) filtering. Circles corresponding to  $1\ell$  and  $4\ell$  of the Gaussian kernel for two representative cells are drawn for comparison. The iterative filter fails to converge in regions where  $\delta\rho$  is small, where the smoothing length becomes very large, and also stops on very different lengths in nearby regions in the mixing layer.

turbulent fluctuations are superimposed on a large-scale variation due to, e.g., the background density profile of the cluster. The expectation is that a successful iterative scheme would be able pick up the small-scale turbulent component and stop the iteration before reaching the smoothly-varying large scales.

We test this scenario in Fig. 8, where we show a synthetic density field initialized on a three-dimensional Voronoi mesh made of a superposition of large-scale modes (representing the background stratification) and small-scale modes, while exponentially suppressed elsewhere. The power is peaked around wave vectors  $kL/(2\pi) \simeq 2 - 4$  and  $15 - 20$ , respectively ( $L$  is the box size). For illustration purposes we compare the iterative filter with a fixed-scale filter whose smoothing length lies between the large- and small-scale bump (cutoff wave number<sup>4</sup> of  $k_c L/(2\pi) = 8$ ) and we repeat the procedure with the spherical

top-hat (for which  $k_c$  corresponds to  $\ell/L \simeq 0.023$ ) and Gaussian smoothing kernels ( $\ell/L \simeq 0.050$ ).

Comparing the turbulent density field reconstructed using the two filtering schemes, we find that iterative filtering yields a small-scale field that still contains residual large-scale modes. We quantify the level of contamination by computing the power spectrum of the resulting density field and comparing it to the original synthetic field (bottom row of Fig. 8). The top-hat kernel appears to perform better in this regard, although the reconstructed turbulent field is more noisy and visually looks less regular. If we look at the distribution of the final filter lengths of the iterative filter (Fig. 9) we find that with the top-hat kernel approximately 27% of the cells have converged to a scale above  $kL/(2\pi) = 4$ , which is where the large-scale bump starts and is well above the scales of the small-scale bump. Similarly, with the Gaussian kernel  $\approx 77\%$  of the cells converged above  $kL/(2\pi) = 4$ , again skipping the small-scale bump.

We conclude that the multiscale iterative filter struggles to distinguish between fluctuations living on widely separated

<sup>4</sup> The cutoff wavelength  $\lambda_c$  and corresponding wave number  $k_c$  were introduced in Section 2. They are defined as the half-width at half-maximum of the smoothing kernel in wavenumber space, allowing us to compare different filtering kernels, see Appendix A for further details.

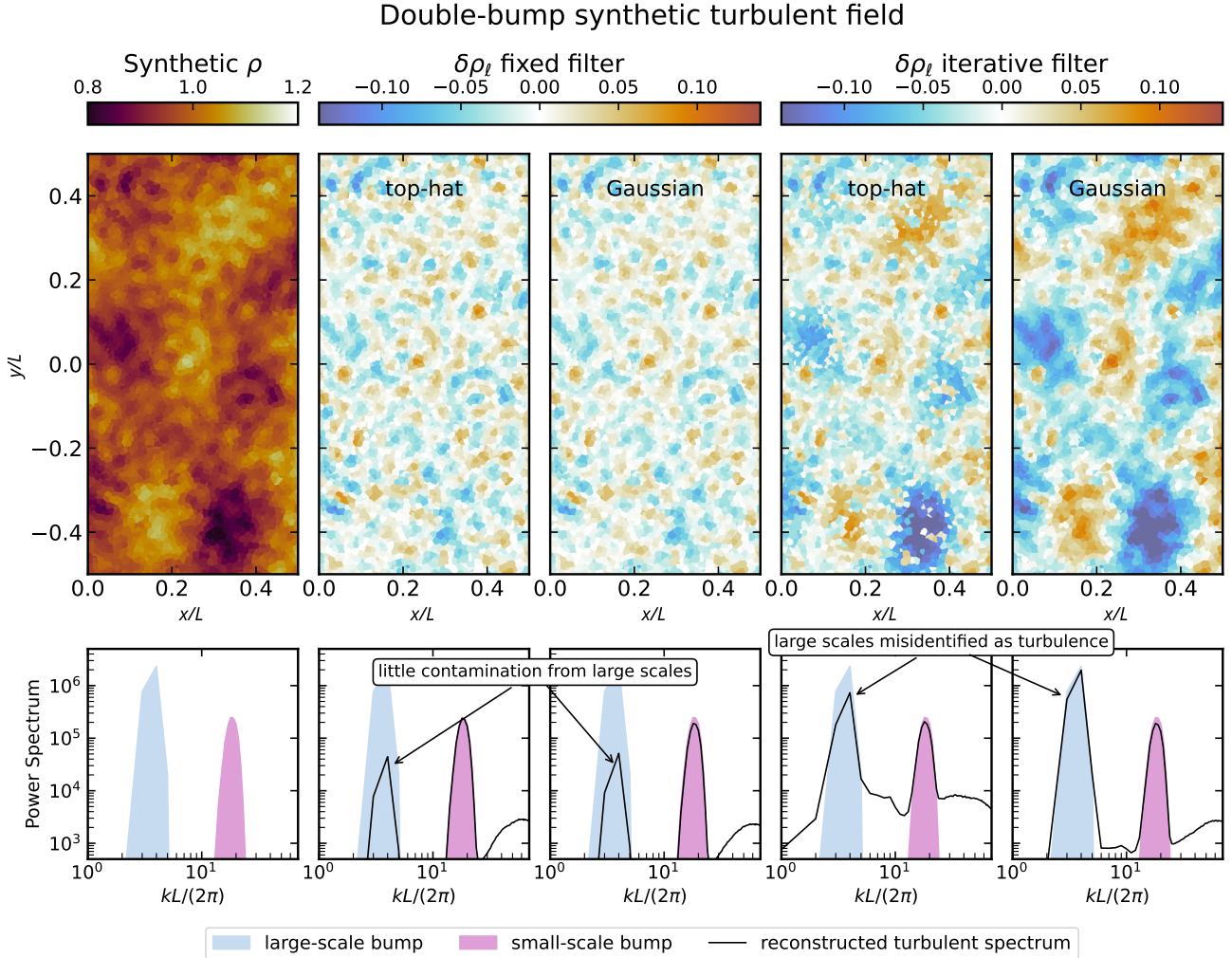


Fig. 8: Comparison of fixed-scale and iterative filtering (tolerance  $\epsilon = 0.05$ ) of a synthetic turbulent density field composed of two “bumps” in Fourier space. Top row, left to right: total density field, reconstructed turbulent field with fixed and iterative filters (both with spherical top-hat and Gaussian kernels). Bottom row: input power spectra of the large- and small-scale bumps (light blue and pink, respectively) and power spectra of the resulting turbulent field after filtering (black line). The excess power at large  $k$  in the reconstructed turbulent spectrum is due to numerical noise after interpolation on a uniform grid. The fixed-scale filters correctly separates the small-scale fluctuations. By contrast, in significant parts of the domain, the iterative filters converge on a scale outside of the spectral break between the two bumps, thus erroneously including large-scale power into the turbulent field.

scales, even with homogeneous turbulence, and instead converges on disparate scales based on the initial conditions.

### 5.3. Alternatives to iterative filters

These considerations should warn against the use of an iterative filter in a realistic ICM environment where such a clean separation between scales is not at all warranted. Moreover, any further quantity obtained from the iteratively filtered fields and integrated over the volume (e.g., kinetic or magnetic turbulent energies, which we define in Section 3) would include contributions from different scales, making its physical interpretation unclear.

On a more conceptual level, as soon as we leave the idealized picture of statistically homogeneous, fully-developed Kolmogorov turbulence – with a single injection scale, an inertial range, and a dissipation scale – an unambiguous and universal definition of what actually constitutes turbulence and what does not is in general not possible. For these reasons, we believe that

the most transparent approach is to use a fixed scale filter with a physically-motivated choice for the smoothing length that is appropriate for the problem and the phenomenon in question, and to repeat this procedure with several filter scales (as we did in Section 4). One tool to aid in the identification of suitable scales is to compute local power spectra. We plan to explore this in detail in future work.

## 6. Conclusions

In this paper, we argue for a method based on smoothing filters to disentangle turbulence in cosmological simulations of galaxy clusters. With this approach, we can separate large-scale fields and small-scale fluctuations based on physical spatial scales, and systematically decompose magnetic and kinetic energies into “bulk” and “turbulent” components. By selecting different smoothing lengths  $\ell$ , we can gain further insight into the properties of the turbulence: for example, the integral scale could be lo-

## Histogram of final convergence scale (iterative)

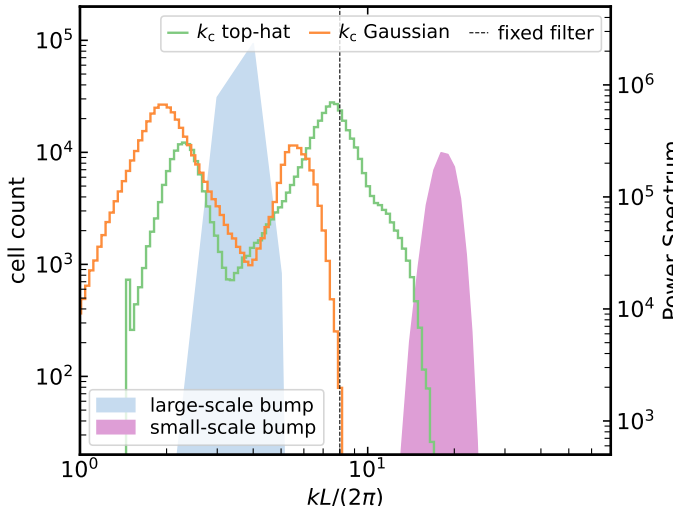


Fig. 9: Distribution of the final convergence scale of the iterative filters (expressed in terms of the cutoff wave vector  $k_c$ ) with spherical top-hat and Gaussian kernels. The vertical black dashed line corresponds to the cutoff wave number of the fixed-scale filter. For comparison we show on the right y-axis the power spectrum of the two bumps as in Fig. 8. A large fraction of the cells converges on scales much larger than the large-scale bump, misidentifying large-scale fluctuations as “turbulence”.

cally estimated by identifying on what scale the turbulent energy stops increasing; moreover, smoothing filters make it possible to study the contribution of different physical processes and energy fluxes across scales. The two main advantages over usual methods based on Fourier transforms are that (a) smoothing filters do not require periodic boundary conditions, they avoid interpolation errors, and can be applied to regions of irregular shape; and (b) that as a result of the filtering, the turbulent (and smooth) fields are available to be used for further analysis, while power spectra or correlation function only yield volume-integrated measures.

We demonstrate the application of smoothing filters and filtered energies to a cosmological simulation of a major cluster merger between two massive clusters (both  $\gtrsim 10^{15} M_\odot$ ) from the PICO-Clusters suite of zoom-in simulations performed with the moving-mesh code AREPO. We follow the evolution of bulk and turbulent energies within  $R_{200,c}$  through the merger until  $z = 0$ . We find that during the merger the turbulent kinetic pressure fraction on physical scales  $\lesssim 160$  kpc reaches about 5% and then quickly decreases to 2% after only  $\sim 1.3$  Gyr from the peak at the core passage (Figure 6). These low turbulent levels are consistent with observations of nearby massive clusters (XRISM Collaboration et al. 2025c) and suggest that, unless the cluster has experienced a major merger in the last 1 – 1.5 Gyr, it will appear as rather quiescent. A more in-depth analysis of the merger will be presented in a separate publication.

In the second part of the paper, we revisit the popular multiscale iterative filtering method, which has been proposed in Vazza et al. (2012) as a technique to automatically distinguish turbulent from bulk motions. We perform a number of tests to evaluate its performance in simple but physically meaningful setups, using two widely used smoothing kernels: the Gaussian, and the spherical top-hat filter. We find that the convergence of iterative multiscale filters does not always seem to reflect the mor-

phology of the physical field either in real or wavenumber space. For example, in simulations of the Kelvin–Helmholtz instability, the iterative filter often converges to very different scales for nearby regions, which produces visible artifacts in the bulk and turbulent fields (Figure 7). On the other hand, in scenarios with fluctuations on two widely separated spatial scales (a factor of  $\sim 10$  in wavelengths), iterative filters struggle to differentiate between small and large-scales fluctuations in a significant fraction of the volume (1/4–3/4 depending on the kernel), and the resulting filtered fields end up containing a mixture of both (Figure 9). In actual simulations of galaxy clusters, we do not expect such wide scale separations, therefore it is unclear how reliable iterative filters would be. Second, the mixing-up of different scales would not allow to decompose the energies into turbulent and bulk, which only makes physical sense in the filter formalism with a fixed scale.

In conclusion, we believe that in complex and heterogeneous systems as the ICM any definition of what constitutes turbulence will always be inherently ambiguous. For this reason, we recommend re-framing this question as a scale-dependent statement, and ask what is the energy (or amplitude) of fluctuations below and above a certain physical scale. With this approach we can make meaningful comparisons across different simulations, and bridge the gap between theory and observations.

## Software

Our filtering code is written in Python (Van Rossum & Drake 2009), and depends on the following packages: PAICOS (Berlok et al. 2024, available at <https://github.com/tberlok/paicos>), NUMPY (Harris et al. 2020), as well as NUMBA (Lam et al. 2015) and CUPY for execution on GPUs. The handling of the AREPO data was done with Paicos, which internally uses ASTROPY (Astropy Collaboration et al. 2013) for units, and employs parallelized routines written in CYTHON (Behnel et al. 2011). Plots were produced with MATPLOTLIB (Hunter 2007), using the CMASHER package for colormaps (van der Velden 2020).

## Acknowledgements

The data underlying this article will be shared on reasonable request to the corresponding author. LMP and CP gratefully acknowledge support by the European Research Council under ERC-AdG grant PICOGAL-101019746. Part of this work was done during a visit at the Niels Bohr Institute funded by the Rosenfeld Foundation. TB gratefully acknowledges funding from the European Union’s Horizon Europe research and innovation programme under the Marie Skłodowska-Curie grant agreement No 101106080. The authors gratefully acknowledge the Gauss Centre for Supercomputing (GCS) for providing computing time on the GCS Supercomputer SuperMUC-NG at the Leibniz Supercomputing Centre (LRZ) in Garching, Germany, under project pn68cu. The Tycho supercomputer hosted at the SCIENCE HPC center at the University of Copenhagen was used for supporting this work.

## References

- Ackermann, M., Ajello, M., Albert, A., et al. 2014, ApJ, 787, 18
- Ackermann, M., Ajello, M., Allafort, A., et al. 2010, ApJ, 717, L71
- Aluie, H. 2011, Phys. Rev. Lett., 106, 174502
- Aluie, H. 2013, Physica D: Nonlinear Phenomena, 247, 54
- Angelinielli, M., Vazza, F., Giocoli, C., et al. 2020, Monthly Notices of the Royal Astronomical Society, 495, 864

Arzamasskiy, L., Kunz, M. W., Squire, J., Quataert, E., & Schekochihin, A. A. 2023, Phys. Rev. X, 13, 021014

Astropy Collaboration, Robitaille, T. P., Tollerud, E. J., et al. 2013, 558, A33

Battaglia, N., Bond, J. R., Pfrommer, C., & Sievers, J. L. 2012, ApJ, 758, 74

Beduzzi, L., Vazza, F., Brunetti, G., et al. 2023, *Astronomy and Astrophysics*, 678, L8

Beduzzi, L., Vazza, F., Cuciti, V., et al. 2024, *Astronomy and Astrophysics*, 690, A67

Behnel, S., Bradshaw, R., Citro, C., et al. 2011, *Computing in Science Engineering*, 13, 31

Beresnyak, A. & Miniati, F. 2016, ApJ, 817, 127

Berlok, T. 2022, *Monthly Notices of the Royal Astronomical Society*, 515, 3492

Berlok, T., Jlassi, L., Puchwein, E., & Haugbølle, T. 2024, *Journal of Open Source Software*, 9, 6296

Berlok, T., Pakmor, R., & Pfrommer, C. 2020, *Monthly Notices of the Royal Astronomical Society*, 491, 2919

Berlok, T. & Pfrommer, C. 2019, *Monthly Notices of the Royal Astronomical Society*, 485, 908

Berlok, T., Quataert, E., Pessah, M. E., & Pfrommer, C. 2021, *Monthly Notices of the Royal Astronomical Society*, 504, 3435

Botteon, A., van Weeren, R. J., Brunetti, G., et al. 2022, *Science Advances*, 8, eabq7623

Bourne, M. A. & Sijacki, D. 2017, MNRAS, 472, 4707

Brunetti, G. & Lazarian, A. 2007, *Monthly Notices of the Royal Astronomical Society*, 378, 245

Carilli, C. L. & Taylor, G. B. 2002, ARA&A, 40, 319

Choudhury, P. P. & Bott, A. F. A. 2025, *Modeling Transport in Weakly Collisional Plasmas Using Thermodynamic Forcing*

Cuciti, V., de Gasperin, F., Brüggen, M., et al. 2022, *Nature*, 609, 911

Dolag, K., Vazza, F., Brunetti, G., & Tormen, G. 2005, *Monthly Notices of the Royal Astronomical Society*, 364, 753

Domínguez-Fernández, P., Vazza, F., Brüggen, M., & Brunetti, G. 2019, *Monthly Notices of the Royal Astronomical Society*, 486, 623

Drake, J. F., Pfrommer, C., Reynolds, C. S., et al. 2021, ApJ, 923, 245

Eckert, D., Ghirardini, V., Ettori, S., et al. 2019, A&A, 621, A40

Ehler, K., Weinberger, R., Pfrommer, C., Pakmor, R., & Springel, V. 2023, MNRAS, 518, 4622

Ehler, K., Weinberger, R., Pfrommer, C., & Springel, V. 2021, MNRAS, 503, 1327

Eyink, G. L. 2007, *Turbulence Theory*, Course Notes (The Johns Hopkins University)

Favre, A. 1983, *Physics of Fluids*, 26, 2851

Frisch, U. 1995, *Turbulence. The Legacy of A.N. Kolmogorov*

Gaspari, M., Churazov, E., Nagai, D., Lau, E. T., & Zhuravleva, I. 2014, *Astronomy and Astrophysics*, 569, A67

Germano, M. 1992, J. Fluid Mech., 238, 325

Grete, P., O’Shea, B. W., Beckwith, K., Schmidt, W., & Christlieb, A. 2017, Phys. Plasmas, 24, 092311

Grete, P., Vlasyuk, D. G., Schmidt, W., Schleicher, D. R. G., & Federrath, C. 2015, New J. Phys., 17, 023070

Groth, F., Valentini, M., Seidel, B. A., et al. 2025, *Turbulence in Simulated Local Cluster Analogs: One-to-One Comparisons between SLOW and XRISM/Hitomi*

Harris, C. R., Millman, K. J., van der Walt, S. J., et al. 2020, *Nature*, 585, 357

Hitomi Collaboration, Aharonian, F., Akamatsu, H., et al. 2016, *Nature*, 535, 117

Hollins, J. F., Sarson, G. R., Evrigen, C. C., et al. 2022, *Geophysical & Astrophysical Fluid Dynamics*, 116, 261

Hunter, J. D. 2007, *Comput. Sci. Eng.*, 9, 90

Iapichino, L., Schmidt, W., Niemeyer, J. C., & Merklein, J. 2011, *Monthly Notices of the Royal Astronomical Society*, 414, 2297

Kida, S. & Orszag, S. A. 1990, J Sci Comput, 5, 85

Komarov, S., Schekochihin, A., Churazov, E., & Spitkovsky, A. 2018, J. Plasma Phys., 84, 905840305

Kunz, M. W., Schekochihin, A. A., Cowley, S. C., Binney, J. J., & Sanders, J. S. 2011, *Monthly Notices of the Royal Astronomical Society*, 410, 2446

Kunz, M. W., Schekochihin, A. A., & Stone, J. M. 2014, Phys. Rev. Lett., 112, 205003

Lam, S. K., Pitrou, A., & Seibert, S. 2015, in Proc. Second Workshop on the LLVM Compiler Infrastructure in HPC, 1–6

Lau, E. T., Gaspari, M., Nagai, D., & Coppi, P. 2017, ApJ, 849, 54

Lau, E. T., Kravtsov, A. V., & Nagai, D. 2009, ApJ, 705, 1129

Lecoanet, D., McCourt, M., Quataert, E., et al. 2016, *Monthly Notices of the Royal Astronomical Society*, 455, 4274

Leonard, A. 1974, *Advances in Geophysics*, 18, 237

Lesieur, M. & Metais, O. 1996, *Annu. Rev. Fluid Mech.*, 28, 45

Ley, F., Zweibel, E. G., Miller, D., & Riquelme, M. 2024, *The Astrophysical Journal*, 965, 155

Li, Y., Gendron-Marsolais, M.-L., Zhuravleva, I., et al. 2020, ApJL, 889, L1

Majeski, S., Kunz, M. W., & Squire, J. 2024, *Journal of Plasma Physics*, 90, 535900601

Meneveau, C. & Katz, J. 2000, *Annu. Rev. Fluid Mech.*, 32, 1

Miniati, F. 2014, ApJ, 782, 21

Miniati, F. 2015, *The Astrophysical Journal*, 800, 60

Monin, A. S. & Yaglom, M. A. 1971, *Statistical Fluid Mechanics: Mechanics of Turbulence*

Pakmor, R., Bauer, A., & Springel, V. 2011, *Monthly Notices of the Royal Astronomical Society*, 418, 1392

Pakmor, R. & Springel, V. 2013, *Monthly Notices of the Royal Astronomical Society*, 432, 176

Pakmor, R., Springel, V., Bauer, A., et al. 2016, *Monthly Notices of the Royal Astronomical Society*, 455, 1134

Perrone, L. M., Berlok, T., & Pfrommer, C. 2024, A&A, 682, A125

Perrone, L. M., Berlok, T., & Pfrommer, C. 2024, *Astronomy and Astrophysics*, 690, A292

Perrone, L. M. & Latter, H. 2022, *Monthly Notices of the Royal Astronomical Society*, 513, 4625

Pillepich, A., Springel, V., Nelson, D., et al. 2018, *Monthly Notices of the Royal Astronomical Society*, 473, 4077

Pinzke, A., Oh, S. P., & Pfrommer, C. 2017, Mon. Not. R. Astron. Soc., 465, 4800

Rajpurohit, K., Botteon, A., O’Sullivan, E., et al. 2025, *The Astrophysical Journal*, 992, 88

Roberg-Clark, G. T., Drake, J. F., Reynolds, C. S., & Swisdak, M. 2018, Phys. Rev. Lett., 120, 035101

Rogallo, R. S. & Moin, P. 1984, *Annual Review of Fluid Mechanics*, 16, 99

Romero, C. E., Gaspari, M., Schellenberger, G., et al. 2024, *The Astrophysical Journal*, 970, 73

Ruszkowski, M. & Pfrommer, C. 2023, A&A Rev., 31, 4

Scannapieco, E. & Brüggen, M. 2008, *Astrophysical Journal*, 686, 927

Schekochihin, A. A. & Cowley, S. C. 2006, *Physics of Plasmas*, 13, 056501

Schekochihin, A. A., Cowley, S. C., Kulsrud, R. M., Hammett, G. W., & Sharma, P. 2005, ApJ, 629, 139

Schekochihin, A. A., Cowley, S. C., Taylor, S. F., Maron, J. L., & McWilliams, J. C. 2004, ApJ, 612, 276

Schmidt, W. 2015, *Living Rev Comput Astrophys.*, 1, 2

Shi, X., Nagai, D., & Lau, E. T. 2018, *Mon Not R Astron Soc.*, 481, 1075

Simionescu, A., ZuHone, J., Zhuravleva, I., et al. 2019, *Space Sci Rev.*, 215, 24

Springel, V. 2010, *Monthly Notices of the Royal Astronomical Society*, 401, 791

Springel, V., Pakmor, R., Pillepich, A., et al. 2018, *Monthly Notices of the Royal Astronomical Society*, 475, 676

Squire, J., Kunz, M. W., Arzamasskiy, L., et al. 2023, *Journal of Plasma Physics*, 89, 905890417

Squire, J., Schekochihin, A. A., Quataert, E., & Kunz, M. W. 2019, J. Plasma Phys., 85, 90585014

St-Onge, D. A., Kunz, M. W., Squire, J., & Schekochihin, A. A. 2020, J. Plasma Phys., 86, 905860503

Su, Y., Kraft, R. P., Roediger, E., et al. 2017, *The Astrophysical Journal*, 834, 74

Tevlin, L., Berlok, T., Pfrommer, C., et al. 2025, *Astronomy and Astrophysics*, 701, A114

Valdarnini, R. 2011, A&A, 526, A158

Valdarnini, R. 2019, ApJ, 874, 42

Vallés-Pérez, D., Planelles, S., & Quilis, V. 2021, *Monthly Notices of the Royal Astronomical Society*, 504, 510

Vallés-Pérez, D., Planelles, S., Quilis, V., et al. 2024, *Computer Physics Communications*, 304, 109305

van der Velden, E. 2020, *The Journal of Open Source Software*, 5, 2004

Van Rossum, G. & Drake, F. L. 2009, *Python 3 Reference Manual* (Scotts Valley, CA: CreateSpace)

Vazza, F. & Brunetti, G. 2025, *On the Interpretation of XRISM X-ray Measurements of Turbulence in the Intracluster Medium: A Comparison with Cosmological Simulations*

Vazza, F., Brunetti, G., Gheller, C., Brunino, R., & Brüggen, M. 2011, A&A, 529, A17

Vazza, F., Jones, T. W., Brüggen, M., et al. 2017, *Monthly Notices of the Royal Astronomical Society*, 464, 210

Vazza, F., Roediger, E., & Brüggen, M. 2012, *Astronomy and Astrophysics*, 544, A103

Walker, S. A., Hlavacek-Larrondo, J., Gendron-Marsolais, M., et al. 2017, *Monthly Notices of the Royal Astronomical Society*, 468, 2506

Walker, S. A., Sanders, J. S., & Fabian, A. C. 2015, Mon. Not. R. Astron. Soc., 453, 3700

Wang, C., Ruszkowski, M., Pfrommer, C., Oh, S. P., & Yang, H.-Y. K. 2021, *Monthly Notices of the Royal Astronomical Society*, 504, 898

Wang, J., Yang, Y., Shi, Y., et al. 2013, Phys. Rev. Lett., 110, 214505

Wang, Q. H. S. & Markevitch, M. 2018, *The Astrophysical Journal*, 868, 45

Wang, Y. & He, P. 2024a, *Monthly Notices of the Royal Astronomical Society*, 528, 3797

Wang, Y. & He, P. 2024b, *The Astrophysical Journal*, 974, 107

Weinberger, R., Springel, V., Hernquist, L., et al. 2017, Mon. Not. R. Astron. Soc., 465, 3291

Weinberger, R., Springel, V., & Pakmor, R. 2020, The Astrophysical Journal Supplement Series, 248, 32

Werner, N., ZuHone, J. A., Zhuravleva, I., et al. 2016, Monthly Notices of the Royal Astronomical Society, 455, 846

XRISM Collaboration, Audard, M., Awaki, H., et al. 2025a, ApJL, 985, L20

XRISM Collaboration, Audard, M., Awaki, H., et al. 2025b, ApJL, 982, L5

XRISM Collaboration, Audard, M., Awaki, H., et al. 2025c, The Astrophysical Journal, 993, L11

XRISM Collaboration, Audard, M., Awaki, H., et al. 2025d, Nature, 638, 365

XRISM Collaboration, Audard, M., Awaki, H., et al. 2025e, Disentangling Multiple Gas Kinematic Drivers in the Perseus Galaxy Cluster

Yang, H.-Y. K. & Reynolds, C. S. 2016, ApJ, 829, 90

Yerger, E. L., Kunz, M. W., Bott, A. F. A., & Spitkovsky, A. 2025, Journal of Plasma Physics, 91, E20

Zhuravleva, I., Churazov, E., Kravtsov, A., et al. 2013, Monthly Notices of the Royal Astronomical Society, 428, 3274

Zhuravleva, I., Churazov, E., Schekochihin, A. A., et al. 2014a, Nature, 515, 85

Zhuravleva, I., Churazov, E., Schekochihin, A. A., et al. 2019, Nat Astron, 3, 832

Zhuravleva, I., Churazov, E. M., Schekochihin, A. A., et al. 2014b, ApJ, 788, L13

ZuHone, J. A., Miller, E. D., Bulbul, E., & Zhuravleva, I. 2018, The Astrophysical Journal, 853, 180

## Appendix A: Comparison of spherical top-hat and Gaussian kernels for iterative filters

In this appendix we discuss two of the most common choices of smoothing kernels, the spherical top-hat, and the Gaussian kernel. We implemented them in our filtering code and tested their convergence properties when used with the iterative multiscale filters.

### A.1. Smoothing kernels in spectral space

We first compare the Fourier transform of the spherical top-hat and Gaussian kernel. We use the convention where the Fourier transform  $\hat{f}(\mathbf{k})$  of a function  $f(\mathbf{x})$  is defined as

$$\hat{f}(\mathbf{k}) = \int_{\mathbb{R}^3} f(\mathbf{x}) e^{-i\mathbf{k}\cdot\mathbf{x}} d^3x. \quad (\text{A.1})$$

In three dimensions the spherical top-hat filter is defined as

$$\mathcal{W}_\ell(\mathbf{x}', \mathbf{x}) = \begin{cases} \left(\frac{4}{3}\pi\ell^3\right)^{-1} & \text{if } |\mathbf{x} - \mathbf{x}'| \leq \ell, \\ 0 & \text{if } |\mathbf{x} - \mathbf{x}'| > \ell, \end{cases} \quad (\text{A.2})$$

while the Gaussian filter is given by

$$\mathcal{W}_\ell(\mathbf{x}', \mathbf{x}) = \frac{1}{(2\pi\ell^2)^{3/2}} e^{-\frac{1}{2}|\mathbf{x} - \mathbf{x}'|^2/\ell^2}. \quad (\text{A.3})$$

These kernels are functions of the single variable  $\mathbf{r} = \mathbf{x}' - \mathbf{x}$  only, thus we will sometimes use the shorthand notation  $\mathcal{W}_\ell(\mathbf{r})$  such that  $\mathcal{W}_\ell(\mathbf{r}) = \mathcal{W}_\ell(\mathbf{x} - \mathbf{x}') = \mathcal{W}_\ell(\mathbf{x}', \mathbf{x})$ , and replace  $\mathbf{r}$  with  $\mathbf{x}$  when there is no risk of ambiguity. Their Fourier transforms can be easily computed, yielding:

$$\hat{\mathcal{W}}_\ell(\mathbf{k}) = \frac{3j_1(k\ell)}{k\ell}, \quad (\text{spherical top-hat}), \quad (\text{A.4})$$

$$\hat{\mathcal{W}}_\ell(\mathbf{k}) = e^{-k^2\ell^2/2}, \quad (\text{Gaussian}), \quad (\text{A.5})$$

where  $j_1(z) = \sin(z)/z^2 - \cos(z)/z$  is the first-order spherical Bessel function of the first kind, and  $k = |\mathbf{k}|$ . We plot the smoothing kernels and their Fourier transform in Fig. A.1 as a function of radius  $r = |\mathbf{x}' - \mathbf{x}|$  and  $k$ , respectively. Both filters have qualitatively similar shapes in Fourier space: when convolved with a function, they suppress Fourier coefficients on scales smaller than  $\ell$ , while leaving those on larger scales unchanged, acting akin to a low-pass filter. Having said that, we note that despite having the same nominal  $\ell$ , the spherical top-hat has a broader half-width at half-maximum (HWHM) than the Gaussian kernel.

Therefore, to compare different filters we compute the HWHM, i.e. the frequency cutoff  $k_c$  at which  $\hat{\mathcal{W}}_\ell(k_c) = 1/2$ . We then convert it into a cutoff wavelength  $\lambda_c = 2\pi/k_c$ . This cutoff wavelength is related to the filter size  $\ell$  by a numerical coefficient which depends on the kernel used. For the spherical top-hat and the Gaussian kernels we have:

$$\frac{\lambda_c}{\ell} = \begin{cases} 2.51503\dots & (\text{spherical top-hat}), \\ 2\pi/\sqrt{2 \ln 2} = 5.33645\dots & (\text{Gaussian}). \end{cases} \quad (\text{A.6})$$

Roughly speaking, we find that for the same  $\ell$  the Gaussian kernel suppresses wavelengths twice as large as the spherical top-hat.

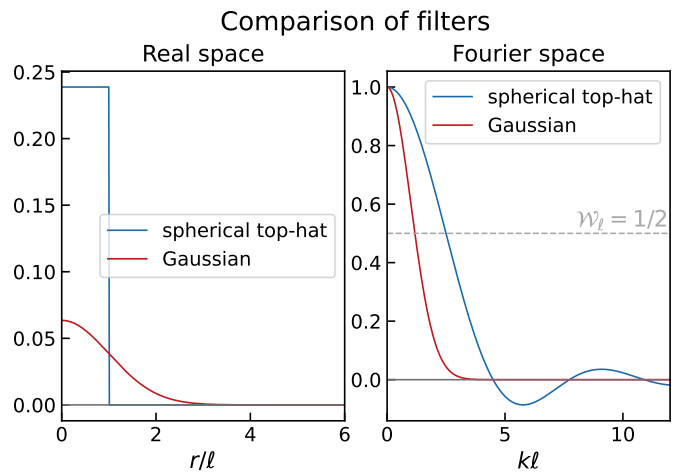


Fig. A.1: Comparison in real (left) and Fourier space (right) between the three-dimensional spherical top-hat and Gaussian filter. The points of intersection between the filter shapes and the  $\mathcal{W}_\ell = 1/2$  line (dashed gray, right panel) represent the half-widths at half-maxima and define the cutoff wavelengths of both filters.

### A.2. Filtering of Fourier series

In this Section we show the action of a smoothing kernel on a generic function. We choose to expand the function in a Fourier series over discrete wave vectors  $\mathbf{k}$  since in all practical applications the domain of interest  $V = L_x L_y L_z$  is finite. However, taking the limit  $V \rightarrow \infty$  and rescaling the Fourier coefficients appropriately, the more general case of continuous  $\mathbf{k}$  is recovered.

We consider a generic periodic function  $f(x)$  expanded in Fourier series:

$$f(\mathbf{x}) = \sum_{\mathbf{k}} \hat{f}_{\mathbf{k}} e^{i\mathbf{k}\cdot\mathbf{x}}, \quad \hat{f}_{\mathbf{k}} = \frac{1}{V} \int_V f(\mathbf{x}) e^{-i\mathbf{k}\cdot\mathbf{x}} d^3x, \quad (\text{A.7})$$

where  $\mathbf{k} = 2\pi \times (n_x/L_x, n_y/L_y, n_z/L_z)^T$ , with  $n_x, n_y, n_z = \dots, -1, 0, 1, \dots$ , and where  $\hat{f}_{\mathbf{k}}$  are the Fourier coefficients. Similarly for the smoothing kernel  $\mathcal{W}_\ell$ :

$$\mathcal{W}(\mathbf{x}) = \sum_{\mathbf{k}} \hat{\mathcal{W}}_{\ell,\mathbf{k}} e^{i\mathbf{k}\cdot\mathbf{x}}. \quad (\text{A.8})$$

The application of a smoothing filter in real space can be represented by a product in Fourier space using the convolution theorem:

$$\begin{aligned} \langle f \rangle_{\ell}(\mathbf{x}) &\equiv \int_V f(\mathbf{x}') \mathcal{W}_\ell(\mathbf{x} - \mathbf{x}') d^3x' \\ &= \sum_{\mathbf{k}} \hat{\mathcal{W}}_{\ell,\mathbf{k}} e^{i\mathbf{k}\cdot\mathbf{x}} \int_V e^{-i\mathbf{k}\cdot\mathbf{x}'} f(\mathbf{x}') d^3x' \\ &= V \sum_{\mathbf{k}} \hat{f}_{\mathbf{k}} \hat{\mathcal{W}}_{\ell,\mathbf{k}} e^{i\mathbf{k}\cdot\mathbf{x}}. \end{aligned} \quad (\text{A.9})$$

where we used the definitions of the Fourier coefficients and the inverse transform in Eq. (A.7)–(A.8). Note that for a kernel with compact support in  $V$ , the Fourier coefficients  $\hat{\mathcal{W}}_{\ell,\mathbf{k}}$  are related to its Fourier transform (Eq. A.1) by  $\hat{\mathcal{W}}_{\ell,\mathbf{k}} = V^{-1} \hat{\mathcal{W}}_\ell(\mathbf{k})$ .

### A.3. Convergence properties

In this section, we examine the convergence properties of the two kernels with the multiscale iterative filter method proposed by Vazza et al. (2012). The multiscale iterative filter operates by successively filtering a scalar or vector field with kernels of increasingly larger size  $\ell_n$  at every iteration, until a certain convergence criterion is met. The final  $\ell_n$  when the iteration is stopped can differ from place to place, and might be identified with the local correlation scale of the turbulence.

In its original formulation (Vazza et al. 2012), for a scalar field  $f(\mathbf{x})$  decomposed as  $f = \langle f \rangle_{\ell_n} + \delta f_{\ell_n}$ , the convergence criterion evaluated at the  $n$ -th iteration is:

$$\left| \frac{\delta f_{\ell_n} - \delta f_{\ell_{n-1}}}{\delta f_{\ell_{n-1}}} \right| \leq \epsilon, \quad (\text{A.10})$$

where  $\epsilon$  is a small tolerance parameter (typically  $\epsilon = 0.02 - 0.1$ ).

While a spherical top-hat filter is used to compute the local bulk and turbulent component in the original work of Vazza et al. (2012), we can show that the Gaussian kernel offers in general better convergence properties. To do so, we first note that if we consider  $\delta f(\ell)$  as a function of the continuous variable  $\ell$ , for small increases of the smoothing length  $\Delta\ell$  the convergence criterion can be equivalently rewritten in terms of the logarithmic derivative of  $\delta f(\ell)$ ,

$$\Delta\ell \left| \frac{d \ln \delta f}{d \ell} \right| \leq \epsilon, \quad \text{for } \delta f \neq 0. \quad (\text{A.11})$$

The criterion above suggests that for  $\epsilon \ll 1$  the iterative algorithm tends to stop at the extrema of the function  $\delta f(\ell)$ . One issue is that, with a spherical top-hat filter, the reconstructed  $\delta f$  at these points is generally not a good approximation of the local turbulent field. This can be clearly seen in the simple case of a single-frequency fluctuation of wavelength  $\lambda$  superimposed on a constant uniform background (Fig. A.2). In this experiment, we sample three representative points (at a maximum of the sine, at a node and at an intermediate value), and numerically compute the values of the smooth field  $\langle f \rangle_{\ell}$  and fluctuation  $\delta f(\ell)$  as a function of  $\ell$  for  $\epsilon = 0.01$ . From Fig. A.2, we can see that when employing a spherical top-hat filter, the iterative algorithm stops near the second extremum of  $\delta f(\ell)$  (for the two non-unity points). Regarding the point at the starting position  $f(x) = 1$ , we note that the expression in Eq. (A.10) becomes singular for  $\delta f(\ell) \simeq 0$ , which is the “true” value given that the sine is odd around that location. In a more realistic scenario, e.g. with discretization error or on a non-uniform grid, the convergence of such points can be dominated by numerical noise. Finally, with the spherical top-hat filter the reconstructed  $\delta f(\ell)$  has an oscillatory behavior (the analytical function has the form of a sinc( $x$ ) =  $\sin(x)/x$ ) and thus converges slowly to the “true” value when  $\ell \gg \lambda$ . With the Gaussian filter, we can get better convergence properties. As shown in the right panel of Fig. A.2, the reconstructed fluctuating field  $\delta f(\ell)$  does not oscillate and converges more quickly (at lower  $\ell$ ) to the true value. This improved behavior, however, comes at the cost of more computations: in fact, for the same  $\ell$ , the support of the Gaussian filter extends much further than the spherical top-hat (we numerically truncate it beyond  $4\ell$  as a compromise between accuracy and speed), which greatly increases the number of operations.

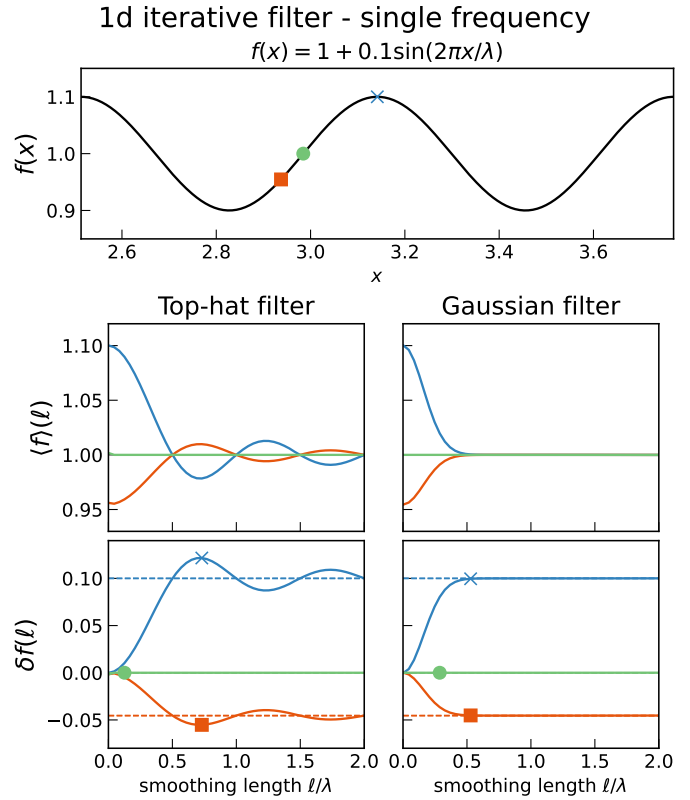


Fig. A.2: One-dimensional test of the convergence criterion in Eq. (A.10) on a uniform grid for  $\epsilon = 0.01$ . The function consists of a constant background plus a sinusoidal perturbation of amplitude  $a = 0.1$  and wavelength  $\lambda = 2\pi/10$ . For the three selected points (colored markers in the top panel), we show the average (middle panel) and fluctuation (bottom panel) for different smoothing lengths  $\ell$ , using a spherical top-hat and Gaussian filter (left and right columns). Bottom panel: the markers indicate where the iterative algorithm stops, the dashed lines the “true” value of the fluctuation at the three selected points. The Gaussian filter has better convergence properties but is more expensive computationally.

## Appendix B: Commutativity between averaging and filtering operators

In this Appendix we discuss under what conditions the volume average,  $\langle \dots \rangle_V$ ,

$$\langle f \rangle_V \equiv \frac{1}{V} \int_V f(\mathbf{x}) d^3x, \quad (\text{B.1})$$

commutes with the filtering operator,  $\langle \dots \rangle_{\ell}$ ,

$$\langle f \rangle_{\ell}(\mathbf{x}) \equiv \int f(\mathbf{x}') W_{\ell}(\mathbf{x}', \mathbf{x}) d^3x'. \quad (\text{B.2})$$

As we will show, this property allows us to recover the total energies (kinetic and magnetic) when using the filtering approach; moreover, it allows us to rule out certain naïve definitions of the turbulent energy density that identically integrate to zero.

### B.1. General considerations about commutativity

In the following section we will restrict ourselves to finite volumes  $V = L_x L_y L_z$ , for which the volume average is well-defined.

We first consider the case of a non-periodic volume  $V$ , where the only conditions on the smoothing kernel are that  $\mathcal{W}_\ell$  is positive-definite, symmetric in its arguments  $(\mathbf{x}, \mathbf{x}')$  and normalized to unity in  $V$ :

$$\int_V \mathcal{W}_\ell(\mathbf{x}, \mathbf{x}') d^3 x' = \int_V \mathcal{W}_\ell(\mathbf{x}', \mathbf{x}) d^3 x' = 1, \quad \forall \mathbf{x} \in V. \quad (\text{B.3})$$

Equation (B.3) implies that, for points  $\mathbf{x}$  near the boundaries of  $V$ , the integration of the kernel  $\mathcal{W}_\ell$  is performed only over the cells belonging to the original volume of interest, without straying beyond it. In this case we have:

$$\begin{aligned} \langle\langle f \rangle_\ell\rangle_V &= \frac{1}{V} \int_V d^3 x \left[ \int_V f(\mathbf{x}') \mathcal{W}_\ell(\mathbf{x}', \mathbf{x}) d^3 x' \right] \\ &= \frac{1}{V} \int_V d^3 x' f(\mathbf{x}') \left[ \int_V \mathcal{W}_\ell(\mathbf{x}', \mathbf{x}) d^3 x \right] \\ &= \frac{1}{V} \int_V d^3 x' f(\mathbf{x}') = \langle f \rangle_V = \langle\langle f \rangle_V \rangle_\ell, \end{aligned} \quad (\text{B.4})$$

where in the last equality we used the fact that applying the filtering operator to a constant leaves its value unchanged. Despite the apparent simplicity of this result, a smoothing kernel that satisfies Eq. (B.3) is computationally hard to implement, as it needs to take into account all the edge cases of the points near the boundaries.

One common approach is to relax the conditions in Eq. (B.3) and assume instead for simplicity that the smoothing kernel is a function of  $(\mathbf{x} - \mathbf{x}')$  only. We then distinguish between the periodic and non-periodic case. If the volume  $V$  is periodic, it is straightforward to verify that the volume average and filtering operators also commute. To show it explicitly, we expand  $f$  and  $\mathcal{W}$  in Fourier series (Eq. A.7), we convolve them using the convolution theorem (Eq. A.9) and, after applying the volume-average operator (Eq. B.1), we obtain

$$\begin{aligned} \langle\langle f \rangle_\ell\rangle_V &= \frac{1}{V} \int_V \left[ V \sum_k \hat{f}_k \hat{\mathcal{W}}_{\ell,k} e^{ik \cdot \mathbf{x}} \right] d^3 x \\ &= V \hat{f}_0 \hat{\mathcal{W}}_{\ell,0}. \end{aligned} \quad (\text{B.5})$$

From the definition of the Fourier series (Eq. A.7) it follows that  $\hat{\mathcal{W}}_{\ell,0} = 1/V$ , since the smoothing kernel is normalized to unity, while  $\hat{f}_0 = \langle f \rangle_V$ . Hence, the volume average and filtering operators commute:

$$\langle\langle f \rangle_\ell\rangle_V = \langle f \rangle_V = \langle\langle f \rangle_V \rangle_\ell. \quad (\text{B.6})$$

When  $V$  is not periodic, the convolution integral must be performed in real space, which means that near the boundaries of  $V$  the smoothing kernel  $\mathcal{W}_\ell$  overlaps with a buffer region  $\delta V$  outside the volume of interest, see Fig. B.1. This region (of thickness  $\sim \ell$ ) must now be included in the integration to correctly normalize the kernel  $\mathcal{W}_\ell$ :

$$\int_{V+\delta V} \mathcal{W}_\ell(\mathbf{x} - \mathbf{x}') d^3 x' = 1, \quad \forall \mathbf{x} \in V, \quad (\text{B.7})$$

and similarly to compute  $\langle\langle f \rangle_\ell\rangle$ . In this case, which is computationally simpler and that we have implemented in our code, the volume average and the smoothing filter do not commute exactly anymore when  $V$  is non-periodic. The difference between  $\langle f \rangle_V$  and  $\langle\langle f \rangle_\ell\rangle_V$  can be given explicitly by first rewriting the volume integral of  $f$  as:

$$\int_V f(\mathbf{x}') d^3 x' = \int_V f(\mathbf{x}') \left[ \int_{V+\delta V} \mathcal{W}_\ell(\mathbf{x} - \mathbf{x}') d^3 x \right] d^3 x', \quad (\text{B.8})$$

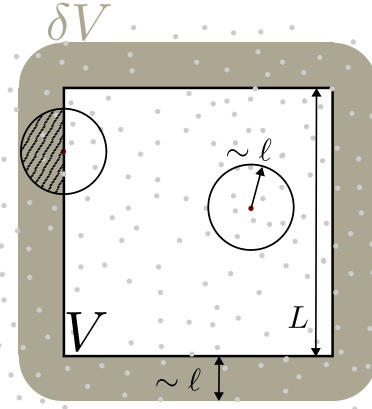


Fig. B.1: Cartoon of the smoothing filters within a finite domain  $V$ . For cells far from the boundaries, all of the support of the smoothing kernel (a ball of radius  $\sim \ell$ ) is contained within  $V$ . For points near the edge and smoothing kernels of the form  $\mathcal{W}_\ell(\mathbf{x} - \mathbf{x}')$ , it is necessary to include a buffer region  $\delta V$  of thickness  $\sim \ell$ .

where we used Eq. (B.7). Similarly for the integral of  $\langle f \rangle_\ell$ :

$$\int_V \langle f \rangle_\ell(\mathbf{x}') d^3 x' = \int_V \left[ \int_{V+\delta V} f(\mathbf{x}') \mathcal{W}_\ell(\mathbf{x}' - \mathbf{x}) d^3 x \right] d^3 x'. \quad (\text{B.9})$$

Splitting the inner integral in Eqs. (B.8)–(B.9) between  $V$  and the buffer volume  $\delta V$  allows to cancel out the integration over  $V$  (since  $\mathbf{x}$  and  $\mathbf{x}'$  are interchangeable within  $V$ ), with only the cross integration remaining. Thus

$$\langle f \rangle_V - \langle\langle f \rangle_\ell\rangle_V = \frac{1}{V} \int_{\delta V} d^3 x \int_V d^3 x' [f(\mathbf{x}') - f(\mathbf{x})] \mathcal{W}_\ell(\mathbf{x} - \mathbf{x}'), \quad (\text{B.10})$$

which involves a double integral that runs over all the pairs  $\mathbf{x} \in V, \mathbf{x}' \in \delta V$  and weighs the difference between the function  $f$  evaluated at these two points. If  $f$  is bounded, it can be shown that Eq. (B.10) scales as  $O(\delta V/V)$ , or  $O(\ell/L)$  for a cubic volume of side  $L$ . In practice, when integrating over the cluster size this difference is usually very small (e.g., we calculated a relative difference of 0.04% for the total kinetic energy shown in Fig. 5a at  $z = 0$ ).

## B.2. Recovering total energies

As we discussed in Section 3, an apparent inconsistency of the filtering approach is that, when we define the filtered bulk and turbulent energy densities their sum does not yield the total energy density. Let us take the example of the magnetic field, for simplicity:  $\varepsilon_{B,\text{bulk}} + \varepsilon_{B,\text{turb}} = \varepsilon_B = \langle e_B \rangle_\ell \neq e_B = \mathbf{B}^2/8\pi$ ; mathematically speaking,  $\varepsilon_B$  corresponds to the filtered version of  $e_B$ . The same applies to the kinetic energy. Using the results of the previous subsection, we can now show that with filtering it is in fact possible to recover the total energy within a volume, which is then repartitioned between bulk and turbulent energy in its entirety.

We will first assume that the volume average and filtering operator commute exactly (which they do if the domain is periodic or if the smoothing kernel  $\mathcal{W}_\ell(\mathbf{x}, \mathbf{x}')$  is symmetric in its arguments and the integration is restricted to  $V$ , see Eq. B.3). We use  $e_\star$  to define either the kinetic or magnetic energy density,

and  $\varepsilon_\star = \langle e_\star \rangle_\ell$  its filtered counterpart. Similarly, their volume integrals are

$$E_\star = \int_V e_\star d^3x, \quad \mathcal{E}_\star = \int_V \varepsilon_\star d^3x. \quad (\text{B.11})$$

Using the volume average in Eq. (B.1), we can write

$$\begin{aligned} \frac{1}{V} \mathcal{E}_\star &= \frac{1}{V} \int_V \varepsilon_\star d^3x = \langle \varepsilon_\star \rangle_V = \langle \langle e_\star \rangle_\ell \rangle_V = \langle \langle e_\star \rangle_V \rangle_\ell \\ &= \frac{1}{V} E_\star \end{aligned} \quad (\text{B.12})$$

where we used Eq. (B.4) to switch the order of the volume average and filtering operator. Thus  $\mathcal{E}_\star = E_\star$ . If the two operators do not commute exactly, the equality can be replaced by an approximate sign ( $\mathcal{E}_\star \simeq E_\star$ ) with a relative error that scales as  $O(\ell/L)$ , see Eq. (B.10).

### B.3. Flawed definition of turbulent energies

Another corollary of the commutativity between volume averaging and smoothing operators is that it allows us to rule out certain naïve definitions of the turbulent energy densities. In fact, considering the kinetic or magnetic energy density  $e_\star$  as a scalar field, one might be tempted to define the difference between  $e_\star$  and its smooth counterpart as a measure of the turbulent energy density, similarly to how one would define the turbulent magnetic or velocity field:  $e_{\star,\text{turb}} \equiv e_\star - \langle e_\star \rangle_\ell$ . However, by virtue of Eq. (B.12), if we integrate this measure over the volume  $V$  we would obtain

$$\int_V e_{\star,\text{turb}} d^3x = E_\star - \mathcal{E}_\star, \quad (\text{B.13})$$

which is either zero (when either  $V$  is periodic or  $\mathcal{W}_\ell$  satisfies Eq. B.3), or asymptotically small.

## Appendix C: Properties of the filtered energies

### C.1. Galilean invariance of the turbulent kinetic energy

In this Appendix we show that the turbulent kinetic energy density ( $\varepsilon_{\text{k,turb}}$ ) as defined in Eq. (23) is Galilean invariant, i.e., it remains constant under a change of frame of reference, while the filtered total kinetic energy density ( $\varepsilon_{\text{k}}$ ), the energy density of the bulk flow ( $\varepsilon_{\text{k,bulk}}$ ), and the transport of turbulent momentum by the bulk flow ( $\varepsilon_{\text{k,cross}}$ ) do not. This result shows that  $\varepsilon_{\text{k,turb}}$  is a physically meaningful measure of the amount of turbulence on small scales.

We place ourselves in a frame of reference moving with uniform velocity  $\mathbf{U}_0$  with respect to the simulation box frame. This could be the center-of-mass velocity of a halo, of multiple pre-merger halos, or another physically-motivated velocity. We define the velocity field in the new frame as  $\mathbf{v}(\mathbf{x}) = \mathbf{u}(\mathbf{x}) - \mathbf{U}_0$  and replace it in Eqs. (19)-(23). Thus, the filtered total kinetic energy density becomes

$$\varepsilon_{\text{k}}(\mathbf{v} + \mathbf{U}_0) = \varepsilon_{\text{k}}(\mathbf{v}) + \frac{1}{2} \langle \rho \rangle_\ell \mathbf{U}_0^2 + \langle \rho \mathbf{v} \rangle_\ell \cdot \mathbf{U}_0, \quad (\text{C.1})$$

while the energy density of the bulk flow is

$$\varepsilon_{\text{k,bulk}}(\mathbf{v} + \mathbf{U}_0) = \varepsilon_{\text{k,bulk}}(\mathbf{v}) + \frac{1}{2} \langle \rho \rangle_\ell \mathbf{U}_0^2 + \langle \rho \rangle_\ell \langle \mathbf{v} \rangle_\ell \cdot \mathbf{U}_0. \quad (\text{C.2})$$

For the transport term  $\varepsilon_{\text{k,cross}}$  we need to calculate the second-order density-velocity moment in terms of the new velocity field  $\mu_2(\rho, \mathbf{v} + \mathbf{U}_0)$ . From the definition of the second-order statistical moment Eq. (10) it is straightforward to show that  $\mu_2(\rho, \mathbf{v} + \mathbf{U}_0) = \mu_2(\rho, \mathbf{v})$ , i.e., it is invariant under a Galilean boost. This also applies to higher-order moments of any argument (i.e., density, velocity, magnetic field, etc.; Germano 1992). The transport term is then simply:

$$\varepsilon_{\text{k,cross}}(\mathbf{v} + \mathbf{U}_0) = \varepsilon_{\text{k,cross}}(\mathbf{v}) + \mathbf{U}_0 \cdot \mu_2(\rho, \mathbf{v}). \quad (\text{C.3})$$

Finally, using Eq. (20) and Eqs. (C.1)-(C.3) or by direct computation, we have

$$\varepsilon_{\text{k,turb}}(\mathbf{v} + \mathbf{U}_0) = \varepsilon_{\text{k,turb}}(\mathbf{v}). \quad (\text{C.4})$$

### C.2. Turbulent kinetic energy in the subsonic regime

In this section, we derive an expression for the turbulent kinetic energy in the subsonic regime. We assume a stably-stratified atmosphere in hydrostatic equilibrium with no mean flow, and perturb the thermodynamic quantities around the background equilibrium:

$$\rho(\mathbf{x}) = \rho_0(\mathbf{x}) + \delta\rho(\mathbf{x}), \quad p(\mathbf{x}) = p_0(\mathbf{x}) + \delta p(\mathbf{x}), \dots \quad (\text{C.5})$$

Note that  $\delta\rho$ ,  $\delta p$ , etc., are not the same as the fluctuations obtained through the application of the smoothing filter:  $\delta\rho \neq \delta\rho_\ell$ . We then take the background thermodynamic quantities  $\rho_0(\mathbf{x})$ ,  $p_0(\mathbf{x})$ ,  $T_0(\mathbf{x})$ , to vary on scales  $H = |\partial \ln \rho_0 / \partial r|^{-1}$  much larger than those of the turbulent fluctuations (in principle, one ought to distinguish between the pressure, density and temperature scale-heights, but for the purpose of this argument we can take them to be all of the same order). If the flow is highly subsonic  $\mathcal{M} = u/c_s \ll 1$ , where  $u$  is the amplitude of the typical velocities, it can be shown (see, e.g., Zhuravleva et al. 2014b) that

$$\frac{\delta\rho}{\rho_0} \sim O(\mathcal{M}) \ll 1. \quad (\text{C.6})$$

We now derive an analogous relation to Eq. (C.6) for the smooth and turbulent density fluctuations obtained with smoothing filters  $\langle \rho \rangle_\ell$ , and  $\delta\rho_\ell = \rho - \langle \rho \rangle_\ell$ , respectively. Our only assumption is that the filter scale  $\ell$  is much smaller than the typical scale-height  $H$ . Applying the smoothing filter to the total density and expanding it as in Eq. (C.5) we have:

$$\begin{aligned} \langle \rho \rangle_\ell(\mathbf{x}) &= \int \rho_0(\mathbf{x}') \mathcal{W}_\ell(\mathbf{x}', \mathbf{x}) d^3x' + \int \delta\rho(\mathbf{x}') \mathcal{W}_\ell(\mathbf{x}', \mathbf{x}) d^3x' \\ &= \int [\rho_0(\mathbf{x}) + (\mathbf{x}' - \mathbf{x}) \cdot \nabla \rho_0(\mathbf{x}) + \dots] \mathcal{W}_\ell(\mathbf{x}', \mathbf{x}) d^3x' + \\ &\quad + \int \delta\rho(\mathbf{x}') \mathcal{W}_\ell(\mathbf{x}', \mathbf{x}) d^3x' \\ &= \rho_0(\mathbf{x}) [1 + O(\ell^2/H^2)] + \int \delta\rho(\mathbf{x}') \mathcal{W}_\ell(\mathbf{x}', \mathbf{x}) d^3x', \end{aligned} \quad (\text{C.7})$$

where in the second line we Taylor-expanded the background density  $\rho_0(\mathbf{x}')$  around  $\mathbf{x}$ , and used the properties of the smoothing kernel (Eq. 1c) to cancel the first term of the Taylor series; finally, we used the fact that  $|\mathbf{x}' - \mathbf{x}| \lesssim \ell$  inside the smoothing integral. As a result, the density fluctuation through the smoothing filter is

$$\begin{aligned} \delta\rho_\ell(\mathbf{x}) &= \rho(\mathbf{x}) - \langle \rho \rangle_\ell(\mathbf{x}) \\ &= \delta\rho(\mathbf{x}) - \int \delta\rho(\mathbf{x}') \mathcal{W}_\ell(\mathbf{x}', \mathbf{x}) d^3x' + O(\ell^2/H^2), \end{aligned} \quad (\text{C.8})$$

and the ratio  $\delta\rho_\ell/\langle\rho\rangle_\ell$  is

$$\frac{\delta\rho_\ell(\mathbf{x})}{\langle\rho\rangle_\ell(\mathbf{x})} = \frac{\delta\rho(\mathbf{x})}{\rho_0(\mathbf{x})} - \int \frac{\delta\rho(\mathbf{x}')}{\rho_0(\mathbf{x})} \mathcal{W}_\ell(\mathbf{x}', \mathbf{x}) d^3x' + O(\ell^2/H^2) + O(\mathcal{M}^2), \quad (\text{C.9})$$

where the leading terms are both of order  $O(\mathcal{M})$ .

We can now take the subsonic limit of turbulent kinetic energy, in which we also include the transport of turbulent momentum by the bulk flow (see Eq. 22–23):

$$\varepsilon_{k,\text{cross}} + \varepsilon_{k,\text{turb}} = \sum_i \langle u_i \rangle_\ell \mu_2(\rho, u_i) + \frac{1}{2} \langle \rho \rangle_\ell \sum_i \mu_2(u_i, u_i) + \frac{1}{2} \sum_i \mu_3(\rho, u_i, u_i). \quad (\text{C.10})$$

We will use the fact that the second- and third-order statistical moments  $\mu_2$  and  $\mu_3$  can be rewritten in integral form as (Eyink 2007; Hollins et al. 2022):

$$\mu_2(\rho, u_i)(\mathbf{x}) = \int [\rho(\mathbf{x}') - \langle \rho \rangle_\ell(\mathbf{x})] \times [u_i(\mathbf{x}') - \langle u_i \rangle_\ell(\mathbf{x})] \mathcal{W}_\ell(\mathbf{x}', \mathbf{x}) d^3x', \quad (\text{C.11})$$

$$\mu_3(\rho, u_i, u_i)(\mathbf{x}) = \int [\rho(\mathbf{x}') - \langle \rho \rangle_\ell(\mathbf{x})] \times [u_i(\mathbf{x}') - \langle u_i \rangle_\ell(\mathbf{x})]^2 \mathcal{W}_\ell(\mathbf{x}', \mathbf{x}) d^3x', \quad (\text{C.12})$$

(note the different arguments  $\mathbf{x}$  and  $\mathbf{x}'$  in the square brackets). Replacing as before  $\rho(\mathbf{x}') = \rho_0(\mathbf{x}') + \delta\rho(\mathbf{x}')$  (Eq. C.5) and expanding  $\rho_0(\mathbf{x}')$  in Taylor series around  $\mathbf{x}$ , we obtain:

$$\mu_2(\rho, u_i)(\mathbf{x}) \simeq \int \delta\rho(\mathbf{x}') [u_i(\mathbf{x}') - \langle u_i \rangle_\ell(\mathbf{x})] \mathcal{W}_\ell(\mathbf{x}', \mathbf{x}) d^3x', \quad (\text{C.13})$$

$$\mu_3(\rho, u_i, u_i)(\mathbf{x}) \simeq \int \delta\rho(\mathbf{x}') [u_i(\mathbf{x}') - \langle u_i \rangle_\ell(\mathbf{x})]^2 \mathcal{W}_\ell(\mathbf{x}', \mathbf{x}) d^3x' - \left( \int \delta\rho(\mathbf{x}') \mathcal{W}_\ell(\mathbf{x}', \mathbf{x}) d^3x' \right) \times \mu_2(u_i, u_i), \quad (\text{C.14})$$

where we neglected terms of order  $O(\ell/H)$ . By simple inspection, we can see that the terms in Eq. (C.13)–(C.14) are both order  $O(\mathcal{M})$  smaller than the leading term in Eq. (C.10):

$$\frac{1}{2} \langle \rho \rangle_\ell \sum_i \mu_2(u_i, u_i) \simeq \frac{1}{2} \rho_0(\mathbf{x}) \sum_i \mu_2(u_i, u_i), \quad (\text{C.15})$$

which we identify with the turbulent kinetic energy in the subsonic regime.

### C.3. Turbulent pressure in the homogeneous subsonic limit

In the filtering approach we define the mean turbulent kinetic pressure  $p_{\text{turb}}$  over a volume  $V$  as:

$$p_{\text{turb}} \equiv \frac{2}{3} \frac{\mathcal{E}_{k,\text{turb}}}{V} = \frac{2}{3} \frac{1}{V} \int_V \varepsilon_{k,\text{turb}}(\mathbf{x}') d^3x'. \quad (\text{C.16})$$

Assuming subsonic turbulence ( $\mathcal{M} \ll 1$ ), the above expression can be approximated as

$$p_{\text{turb}} \simeq \frac{1}{3} \frac{1}{V} \int_V \rho_0(\mathbf{x}') \sigma_{3D,u}^2(\mathbf{x}') d^3x' \quad (\text{C.17})$$

where we used the subsonic limit of the turbulent energy density in Appendix C.2, and defined the three-dimensional local velocity dispersion  $\sigma_{3D,u}$  as  $\sigma_{3D,u}^2(\mathbf{x}) = \sum_i \mu_2(u_i, u_i)$  (we will drop the subscript “ $u$ ” for readability). If the turbulence is homogeneous in the volume  $V$ , the background quantities and the statistical properties of the fields do not depend on  $\mathbf{x}$ . This implies that  $\rho_0 \simeq \text{const}$ , and the turbulent kinetic pressure reduces to

$$p_{\text{turb}} \simeq \frac{1}{3} \rho_0 \sigma_{3D,\text{rms}}^2, \quad (\text{C.18})$$

where we defined the rms velocity dispersion  $\sigma_{3D,\text{rms}}$  as

$$\sigma_{3D,\text{rms}}^2 \equiv \frac{1}{V} \int_V \sigma_{3D}^2(\mathbf{x}') d^3x'. \quad (\text{C.19})$$

If the turbulence is isotropic, then the volume averages of  $\mu_2(u_x, u_x)$ ,  $\mu_2(u_y, u_y)$  and  $\mu_2(u_z, u_z)$  are the same, and we can define a one-dimensional rms velocity dispersion  $\sigma_{1D,\text{rms}}$  as

$$\sigma_{1D,\text{rms}}^2 \equiv \frac{1}{3} \sigma_{3D,\text{rms}}^2, \quad (\text{C.20})$$

whereby the turbulent pressure becomes  $p_{\text{turb}} \simeq \rho_0 \sigma_{1D,\text{rms}}^2$ .

## Appendix D: The TURBOCLUSTER library

We implement the spherical top-hat and Gaussian smoothing filters and the computation of the filtered energies in a new Python library called TURBOCLUSTER, which uses NVIDIA graphical processing units (GPUs) to speed up computations using the NUMBA library. Our code partially depends on Paicos, which is a Python software package for visualizing and analyzing AREPO simulations, but it is written in a way that it can easily be adapted to any simulation data that can be read in as a set of cell positions, volumes and associated physical quantities to be smoothed (e.g. density, velocity field, …). We plan to release the TURBOCLUSTER library publicly in the near future.

### D.1. Neighbor search with Cartesian tiling

An AREPO snapshot for a simulation with  $N$  gas cells contains their positions, but not their spatial connectivity. The main computational burden of applying a smoothing filter is thus to select the cells inside the spherical search radius  $r_s$  of a cell ( $r_s$  is related to the spherical top-hat and Gaussian smoothing length  $\ell$  by  $r_s = \ell$  and  $r_s = 4\ell$ , respectively). In computer science, this problem is known as a range search, which is related to the nearest neighbor problem. It is well known that the brute-force approach for finding the nearest neighbor of a point in space requires  $O(N^2)$  distance comparisons, but spatial trees can reduce the algorithmic complexity to  $O(N \log N)$ . We have opted for a simpler approach, i.e., we select a cubic region with side length  $L$  that encompasses a region of interest (e.g., the volume within  $R_{200,c}$ ) and divide it into  $M^3$  cubic sub-regions with side lengths  $d = L/M$  that we call “tiles”. Using this Cartesian tiling, we index and sort the cells based on the tile in which their mesh-generating points are located. This indexing has algorithmic complexity  $O(N)$  and the sorting, which uses an implementation of radix sort from the Thrust library (called via CUPY), is also extremely fast in practice. With this approach, the number of distance comparisons necessary for smoothing filters is reduced significantly (see below for further details).

For a set of uniformly distributed points<sup>5</sup> with mean number density of cells  $n = N/L^3$ , each tile contains on average  $N_t = N/M^3 = nd^3$  points. We then introduce a search efficiency (or hit ratio)  $\eta$ , measured as the number of cells found inside the search radius divided by the number of distance comparisons. For example, with the brute-force approach, we need  $\approx N^2$  evaluations, so the efficiency is

$$\eta = \frac{N(< r_s)}{N^2} \approx \frac{4.19}{N} \left( \frac{r_s}{L} \right)^3, \quad (\text{D.1})$$

where we used that, on average,  $N(< r_s) = 4\pi r_s^3 n/3$ . With Cartesian tiling, for a given search radius  $r_s$ , we only need to search for neighbors in the tiles that overlap (all or in part) with a sphere of radius  $r_s$  centered on the point of interest  $x_0$ . For small search radii ( $\leq d/2$ ), the worst case scenario is when  $x_0$  is located near the corner of a tile, in which case multiple tiles have to be checked. In this case, one needs to make at most  $8N_t$  evaluations to find the cells contained inside  $r_s$  and the worst case efficiency is

$$\eta = \frac{N(< r_s)}{8N_t} \approx 0.52 \left( \frac{r_s}{d} \right)^3, \quad (\text{D.2})$$

which for  $r_s = d/2$  gives  $\eta \approx 0.065$ . However, as the ratio  $r_s/d$  increases, the position of  $x_0$  with respect to the tile edges and corners matters less, and the efficiency of Cartesian tiling increases, since smaller cubic tiles can better approximate a sphere of radius  $r_s$ . For  $r_s \gg d$ ,  $\eta \rightarrow 1$ .

We measure the efficiency of our algorithm for *Hal03* at  $z = 0$ , selecting a cubic region of size  $L \approx 1.49$  Mpc. We then apply the smoothing filter with spherical top-hat kernel and  $\ell = \{30, 60, 90, 120, 150, 240\}$  kpc, equal to the search radius, and for different tiling parameter  $M = \{64, 128, 256, 512\}$ . For each pair  $(\ell, M)$ , we compute the efficiency  $\eta$ , and plot it against  $r_s/d$  in Fig. D.1. We also numerically determine the expected efficiency as a function of  $r_s/d$  for a uniform distribution of randomly-drawn points in a three-dimensional Cartesian grid; the median and  $1\sigma$  standard deviation are shown in Fig. D.1 for comparison. As we can see, the theoretical expectation for a uniform distribution of points and the measured efficiency of our Cartesian tiling agree very well, which confirms the correctness of our implementation, and suggests that, within  $L \approx 1.49$  Mpc, the density of mesh-generating points is relatively homogeneous on the filter length scales employed here.

## D.2. Timing benchmarks

We perform a number of timing tests on the  $z = 0$  snapshot of *Hal03*, using an NVIDIA A100 GPU. We keep the size of the cubic region fixed ( $L = 2R_{200,c} \approx 5.9$  Mpc), and filter the data using three filter scales  $\ell = \{15, 30, 59\}$  kpc, as in Section 4.3, both with spherical top-hat and with Gaussian kernels. This selection contains  $N \approx 39 \times 10^6$  mesh-generating points of our computational Voronoi cells, with a median spatial resolution of  $\approx 15$  kpc (assuming they are of spherical shape, see Fig. D.2). This suggests that, for the spherical top-hat and for the lowest filter scale, in about 50% of the cases the search radius around the cell is actually empty. From a physical perspective such a scenario should be avoided. For the Gaussian kernel, on the other hand, even for

<sup>5</sup> In cosmological simulations with moving-mesh or smoothed particle-hydrodynamics codes, the gas cell positions are not uniformly distributed; rather, they follow the gas density distribution imposed by large-scale structure and galaxy formation.

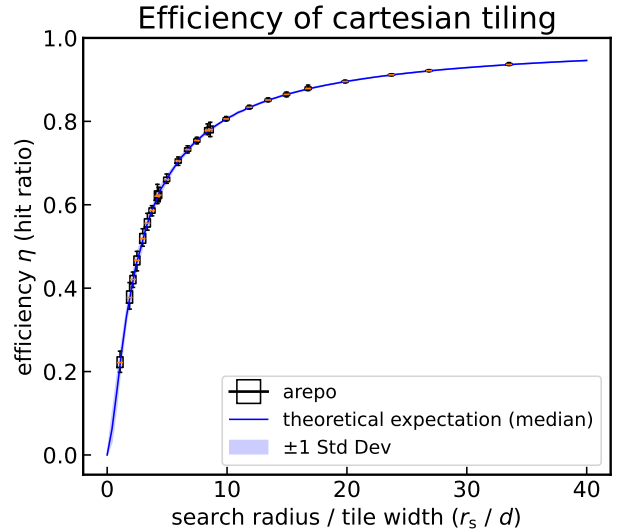


Fig. D.1: Cartesian tiling efficiency. The squares with error bars have been obtained by filtering a cubic region of size  $L \approx 1.49$  Mpc centered on the center of *Hal03*, and for different combinations of filter sizes  $\ell$  and tiling parameter  $M$ . The solid blue line and shaded region represent the expected efficiency for a uniform random distribution of points (median value and one standard deviation, respectively).

$\ell = 15$  kpc, the search radius is 60 kpc, which is inadequate only for a low number of cells in the cluster outskirts.

Using our default parameters ( $M = 256$ , for which  $d \approx 23$  kpc), it takes 20.4 (0.4) seconds to apply a Gaussian (spherical top-hat) smoothing filter for the intermediate scale  $\ell = 30$  kpc. These timings increase substantially for the largest scale  $\ell = 59$  kpc, particularly for the Gaussian kernel (137.4 s), which by construction has a search radius four times as large as  $\ell$ . We repeat this procedure using different values of  $M = \{64, 128, 256, 512\}$  for the Cartesian tiling, in order to assess whether there is an optimal choice that minimizes the execution time. As it turns out,  $M = 256$  indeed represents the value for which the execution time is lowest, while choosing  $M < 256$  and  $M = 512$  leads to longer execution. This makes intuitive sense, since for  $M = 512$  the total number of Cartesian tiles becomes higher than the number of particles in our selection: as a result many tiles end up being empty, and computational resources are wasted looping over empty tiles. On the contrary, if  $M$  is too small, the ratio  $r_s/d$  decreases, and neighbor searching using Cartesian tiling is less efficient (see Fig. D.1).

## Appendix E: Turbulent energies in non-periodic domains

In this Appendix, we extend the results of Section 3.4.2 to the case of non-periodic volumes. For simplicity, we consider smaller Cartesian sub-volumes  $V^{(i)}$  of a larger periodic parent box  $V$ , which is the more likely scenario when analyzing cosmological simulations. As in Section 3.4.2, we focus on the turbulent magnetic energy, but the following results also apply with minor modifications to the turbulent kinetic energy in the sub-sonic limit. We first expand the magnetic field in a Fourier series

Table D.1: Benchmark of smoothing filter with an NVIDIA A100 GPU.

$M$	$\ell = 15 \text{ kpc}$	$\ell = 30 \text{ kpc}$	$\ell = 59 \text{ kpc}$
64	13.3 (2.5)	46.1 (3.1)	218.9 (8.4)
128	5.6 (0.4)	26.5 (0.9)	158.1 (3.0)
256	3.5 (0.1)	20.4 (0.4)	137.4 (1.7)
512	3.9 (0.1)	27.3 (0.4)	194.5 (2.1)

**Notes.** Timings in seconds of the smoothing filter applied to `Hal03` at  $z = 0$ , for different grid sizes of the Cartesian tiling ( $M$ ) and for different smoothing lengths ( $\ell$ ). The values quoted in the Table refer to the application of a Gaussian filter, with the spherical top-hat filter in brackets. The region filtered is a cube of size  $L = 2R_{200,c} \simeq 5.9 \text{ Mpc}$ .

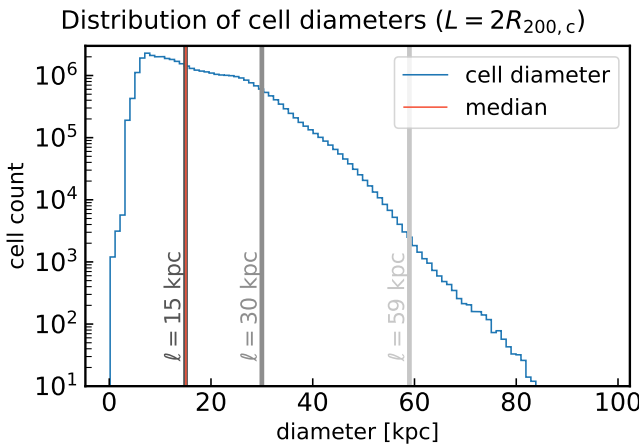


Fig. D.2: Histogram of the cell diameters inside a cubic region of  $L = 2R_{200,c}$  centered on the cluster center. The vertical red line represents the median of the distribution, while the solid gray lines indicate the filter scales used with the Gaussian and spherical top-hat kernel.

in  $V$ :

$$\mathbf{B}(\mathbf{x}) = \sum_{\mathbf{k}} \hat{\mathbf{B}}_{\mathbf{k}} e^{i\mathbf{k} \cdot \mathbf{x}}, \quad (\text{E.1})$$

where the Fourier coefficients are divergence-free. Following closely the steps in Eq. (28)–(30), we use the convolution theorem (Eq. A.9) and the definition of  $\varepsilon_{B,\text{turb}}$  (Eq. 12) to write the turbulent magnetic energy density at every point  $\mathbf{x} \in V$ , which is the same as in Eq. (31), and is reported below for convenience:

$$8\pi\varepsilon_{B,\text{turb}}(\mathbf{x}) = \sum_{\mathbf{k}} |\hat{\mathbf{B}}_{\mathbf{k}}|^2 (1 - |\tilde{\mathcal{W}}_{\ell,\mathbf{k}}|^2) + \sum_{\mathbf{k} \neq \mathbf{k}'} \hat{\mathbf{B}}_{\mathbf{k}}^* \cdot \hat{\mathbf{B}}_{\mathbf{k}'} e^{i(\mathbf{k}' - \mathbf{k}) \cdot \mathbf{x}} [\tilde{\mathcal{W}}_{\ell,\mathbf{k}' - \mathbf{k}} - \tilde{\mathcal{W}}_{\ell,\mathbf{k}} \tilde{\mathcal{W}}_{\ell,\mathbf{k}' }]. \quad (\text{E.2})$$

In contrast to Section 3.4.2, we now integrate  $\varepsilon_{B,\text{turb}}$  over a sub-volume  $V^{(i)}$  of cubic shape contained in  $V$ , defined by its center  $\mathbf{r}^{(i)}$  and extension  $L_x^{(i)}$ ,  $L_y^{(i)}$  and  $L_z^{(i)}$  in the three dimensions, respectively. Integration of the turbulent energy density Eq. (E.2) now yields two terms: one resulting from the first term (a constant), and a contribution from the second term which is now non-vanishing (in general), and depends on the location of the

sub-volume,

$$\begin{aligned} \varepsilon_{B,\text{turb}}(\mathbf{r}^{(i)}; V^{(i)}) &= \sum_{\mathbf{k}} \frac{|\hat{\mathbf{B}}_{\mathbf{k}}|^2}{8\pi} (1 - |\tilde{\mathcal{W}}_{\ell,\mathbf{k}}|^2) V^{(i)} \\ &+ \sum_{\mathbf{k} \neq \mathbf{k}'} \frac{\hat{\mathbf{B}}_{\mathbf{k}}^* \cdot \hat{\mathbf{B}}_{\mathbf{k}'}}{8\pi} [\tilde{\mathcal{W}}_{\ell,\mathbf{k}' - \mathbf{k}} - \tilde{\mathcal{W}}_{\ell,\mathbf{k}} \tilde{\mathcal{W}}_{\ell,\mathbf{k}'}] \\ &\times \left[ \prod_{j=x,y,z} \text{sinc}\left(\frac{(\mathbf{k}' - \mathbf{k})_j L_j^{(i)}}{2}\right) \right] \cos((\mathbf{k}' - \mathbf{k}) \cdot \mathbf{r}^{(i)}) V^{(i)}, \quad (\text{E.3}) \end{aligned}$$

where we introduced the sinc function as  $\text{sinc}(z) = \sin(z)/z$ . The second term represents interference between different modes and can be either constructive or destructive. Note that a similar situation would arise if we were to compute the total magnetic energy in  $V^{(i)}$  from Eq. (E.1) without any filtering.

In the interference term in Eq. (E.3) both large-scale modes (with respect to  $\ell$ ) and small-scale modes can contribute. However, based on some general considerations, we can show that it is the small-scale modes that give the largest contribution. We focus our attention on the attenuation term due to filtering:

$$\tilde{\mathcal{W}}_{\ell,\mathbf{k}' - \mathbf{k}} - \tilde{\mathcal{W}}_{\ell,\mathbf{k}} \tilde{\mathcal{W}}_{\ell,\mathbf{k}'}. \quad (\text{E.4})$$

We can distinguish three cases: (i) both wave vectors in the double summation are large-scale  $|\mathbf{k}| \sim |\mathbf{k}'| \ll 1/\ell$ ; (ii) both small-scale  $|\mathbf{k}| \sim |\mathbf{k}'| \gg 1/\ell$ ; (iii) one is large-scale and one small-scale ( $|\mathbf{k}| \ll 1/\ell \ll |\mathbf{k}'|$  without loss of generality). We examine them below in turn:

- when both wave vectors are large-scale,  $\tilde{\mathcal{W}}_{\ell,\mathbf{k}} \approx \tilde{\mathcal{W}}_{\ell,\mathbf{k}'}$   $\approx 1$ , and their difference is also small:  $|\mathbf{k}' - \mathbf{k}| \ll 1/\ell$ ; this implies  $\tilde{\mathcal{W}}_{\ell,\mathbf{k}' - \mathbf{k}} \approx 1$  and the attenuation term (Eq. E.4) is approximately zero, thus large-scale modes contribute little;
- when both wave vectors are small-scale,  $\tilde{\mathcal{W}}_{\ell,\mathbf{k}} \approx \tilde{\mathcal{W}}_{\ell,\mathbf{k}'} \approx 0$ , but  $\tilde{\mathcal{W}}_{\ell,\mathbf{k}' - \mathbf{k}}$  can still be approximately 1 if  $\mathbf{k}' \approx \mathbf{k}$  (although they cannot be exactly equal), and contribute to the interference term;
- the final case where wave vectors are mixed also does not contribute significantly: the product  $\tilde{\mathcal{W}}_{\ell,\mathbf{k}} \tilde{\mathcal{W}}_{\ell,\mathbf{k}'}$  is approximately zero (since  $\tilde{\mathcal{W}}_{\ell,\mathbf{k}'} \approx 0$ , and  $|\mathbf{k}' - \mathbf{k}| \approx |\mathbf{k}'| \gg 1/\ell$ , thus  $\tilde{\mathcal{W}}_{\ell,\mathbf{k}' - \mathbf{k}} \approx 0$ ). Therefore mixed modes also do not contribute significantly.

To summarize, we expect most of the contribution to the interference term in the turbulent energy to come from small-scale modes: this makes physical sense and agrees with the notion that, for a double product like the magnetic energy, or the kinetic energy in the subsonic limit, only fluctuations on scales smaller than  $\ell$  should enter in the turbulent energy (for compressible turbulence, contributions from mixed large- and small-scale modes are in general unavoidable). In particular, we could imagine that modes with very similar wave vectors are more correlated than those with dissimilar wave vectors; for these correlated modes, there would be little cancellation in the double summation in Eq. (E.3), thus leading to a large contribution to the turbulent energy. If, on the other hand, the Fourier modes are uncorrelated, the interference term would be minimized.

We can test our hypothesis by initializing a synthetic magnetic field as in Section 3.4.2, whose power spectrum follows a known power-law (in this case Kolmogorov), and with uncorrelated Fourier amplitudes, see Fig. E.1. We then randomly select 10 non-periodic Cartesian sub-volumes  $V^{(i)}$ , with  $i = 0, \dots, 9$ ,

Synthetic magnetic field (sub-volumes)

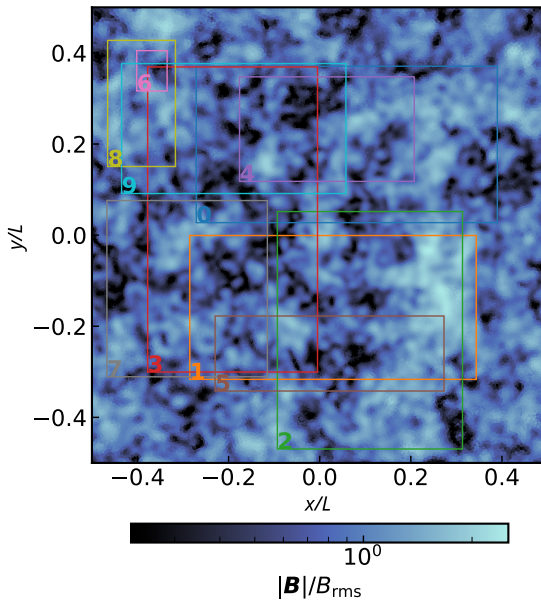


Fig. E.1: Two-dimensional slice of a three-dimensional turbulent synthetic magnetic field (same as in Fig. 3a). Overplotted are the cross-sections of the sub-volumes as seen in projection.

and compute the total  $\mathcal{E}_B^{(i)}$ , bulk  $\mathcal{E}_{B,\text{bulk}}^{(i)}$  and turbulent filtered energies  $\mathcal{E}_{B,\text{turb}}^{(i)}$  for different filter scales  $\ell$ , which we plot in Fig. E.2. Since the sub-volumes are of various sizes, the total energy in each of them can in principle be different. However, because the magnetic field is statistically homogeneous, we expect the mean energy density in each sub-volume  $\mathcal{E}_B^{(i)}/V^{(i)}$  to scatter around the mean value in  $V$ . On the other hand, if the Fourier modes are indeed uncorrelated, we predict the mean turbulent magnetic energy density in each sub-volume  $\mathcal{E}_{B,\text{turb}}^{(i)}/V^{(i)}$  to be the same for all sub-volumes for each  $\ell$  according to Eq. (E.3), and equal to the energy contained in the power spectrum, with large-scale modes suppressed by the smoothing kernel:

$$\frac{\mathcal{E}_B^{(i)}}{V^{(i)}} \simeq \sum_k \frac{|\hat{\mathbf{B}}_k|^2}{8\pi} (1 - |\tilde{\mathcal{W}}_{\ell,k}|^2). \quad (\text{E.5})$$

Indeed, by looking at Fig. E.2, we see that the turbulent mean energy densities closely follow the theoretical expectation based on Eq. (E.5), despite the relatively larger scatter of the total and bulk energy densities.

Normalized mean energy density (sub-volumes)

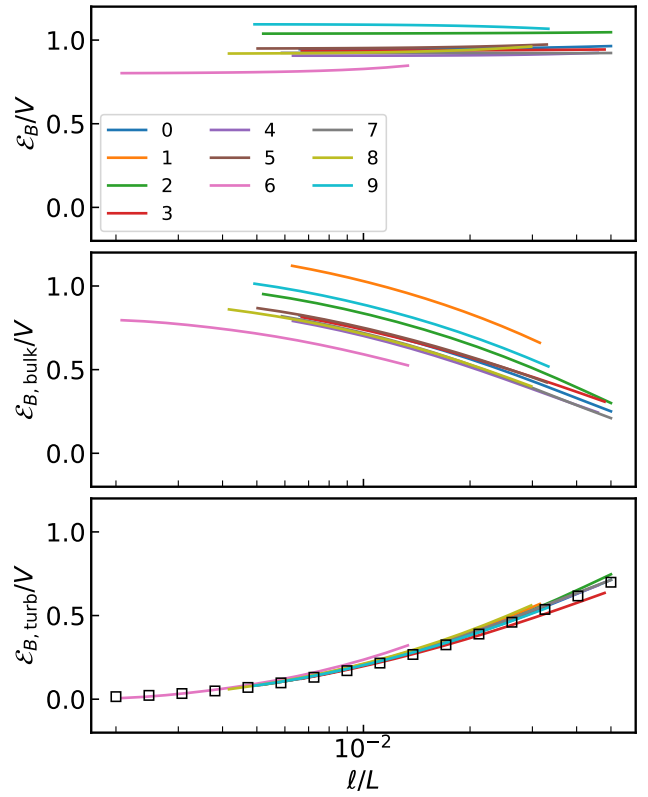


Fig. E.2: Filtered total (top), bulk (middle) and turbulent (bottom) magnetic energies in small non-periodic sub-volumes (see Fig. E.1 for a slice of the turbulent magnetic field and a cross-section of the sub-volumes). Since the Fourier modes are uncorrelated, the interference term due to non-periodic boundaries is very small, and the mean turbulent energy density is approximately the same in all sub-volumes.